UC San Diego
UC San Diego Previously Published Works

Title

Context-dependent roles of mitochondrial LONP1 in orchestrating the balance between airway progenitor versus progeny cells

Permalink

https://escholarship.org/uc/item/01f831dn

Authors

Xu, Le
Tan, Chunting
Barr, Justinn
<u>et al.</u>

Publication Date

2024-08-01

DOI

10.1016/j.stem.2024.08.001

Copyright Information

Peer reviewed

Context-dependent roles of mitochondrial LONP1 in orchestrating the balance between airway progenitor versus progeny cells

Graphical abstract
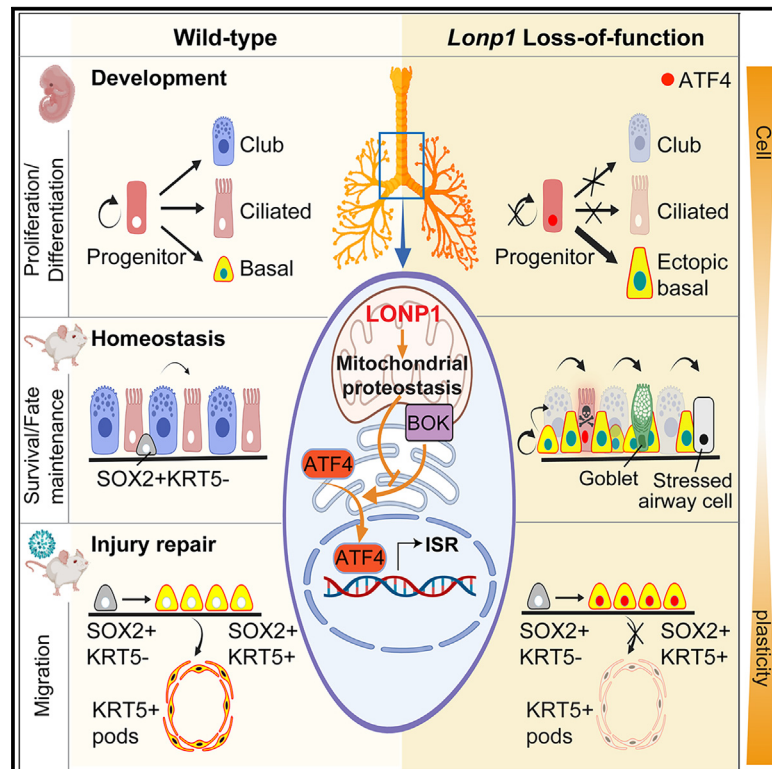
Authors

Le Xu, Chunting Tan, Justinn Barr, ..., Wendy K. Chung, David J. McCulley, Xin Sun

Correspondence

xinsun@health.ucsd.edu

In brief

Xu et al. found that inactivation of *Lonp1*, a mitochondrial protease gene, in the mouse lung led to mitochondrial deficiency, with differential outcomes depending on the context. Mitochondrial deficiency acts through BOK and the integrated stress response pathway to trigger progenitor/progeny cell imbalance at baseline and failed progenitor migration following viral injury.

Highlights

- Airway cells show context-dependent sensitivity to mitochondrial deficiency

- Mitochondrial deficiency impacts cell behavior via the integrated stress response

- BOK expression predicts cells with elevated sensitivity to mitochondrial deficiency

- Mitochondria-deficient airways show progenitor/progeny imbalance, mimicking COPD

CellPress

Cell Stem Cell

CellPress

Article

Context-dependent roles of mitochondrial LONP1 in orchestrating the balance between airway progenitor versus progeny cells

Le Xu,[1] Chunting Tan,[1,12] Justinn Barr,[1] Nicole Talaba,[1] Jamie Verheyden,[1] Ji Sun Chin,[1] Samvel Gaboyan,[2,3] Nikita Kasaraneni,[2,3] Ruth M. Elgamal,[1] Kyle J. Gaulton,[1] Grace Lin,[6] Kamyar Afshar,[3] Eugene Golts,[4] Angela Meier,[5] Laura E. Crotty Alexander,[2,3] Zea Borok,[3] Yufeng Shen,[7,8,9] Wendy K. Chung,[10] David J. McCulley,[1] and Xin Sun[1,11,13,*]

[1]Department of Pediatrics, School of Medicine, University of California, San Diego, La Jolla, CA 92093, USA
[2]Pulmonary and Critical Care Section, Veterans Affairs San Diego Healthcare System, La Jolla, CA, USA
[3]Division of Pulmonary, Critical Care and Sleep Medicine, Department of Medicine, University of California, San Diego, La Jolla, CA, USA
[4]Department of Surgery, Division of Cardiovascular and Thoracic Surgery, University of California, San Diego, La Jolla, CA, USA
[5]Department of Anesthesiology, Division of Critical Care, University of California, San Diego, La Jolla, CA, USA
[6]Department of Pathology, University of California, San Diego, La Jolla, CA, USA
[7]Department of Systems Biology, Columbia University Irving Medical Center, New York, NY 10032, USA
[8]Department of Biomedical Informatics, Columbia University Irving Medical Center, New York, NY 10032, USA
[9]JP Sulzberger Columbia Genome Center, Columbia University Irving Medical Center, New York, NY 10032, USA
[10]Department of Pediatrics, Boston Children's Hospital and Harvard Medical School, Boston, MA 02115, USA
[11]Department of Cell and Developmental Biology, University of California, San Diego, La Jolla, CA 92093, USA
[12]Present address: Department of Respiratory Medicine, Beijing Friendship Hospital, Capital Medical University, Beijing, China
[13]Lead contact
*Correspondence: xinsun@health.ucsd.edu
https://doi.org/10.1016/j.stem.2024.08.001

SUMMARY

While all eukaryotic cells are dependent on mitochondria for function, in a complex tissue, which cell type and which cell behavior are more sensitive to mitochondrial deficiency remain unpredictable. Here, we show that in the mouse airway, compromising mitochondrial function by inactivating mitochondrial protease gene *Lonp1* led to reduced progenitor proliferation and differentiation during development, apoptosis of terminally differentiated ciliated cells and their replacement by basal progenitors and goblet cells during homeostasis, and failed airway progenitor migration into damaged alveoli following influenza infection. ATF4 and the integrated stress response (ISR) pathway are elevated and responsible for the airway phenotypes. Such context-dependent sensitivities are predicted by the selective expression of *Bok*, which is required for ISR activation. Reduced LONP1 expression is found in chronic obstructive pulmonary disease (COPD) airways with squamous metaplasia. These findings illustrate a cellular energy landscape whereby compromised mitochondrial function could favor the emergence of pathological cell types.

INTRODUCTION

The human airway is composed of a rich array of cell types, each with specialized function.[1–4] A balanced ratio of progenitor versus progeny cells is essential for proper airway function. Airway epithelium is also a source of progenitors that can migrate into the alveolar region following influenza infection.[5–7] How the optimal balance of airway progenitor and progeny cell types is established, maintained, and restored remains poorly understood.

Aside from their canonical role as the energy source of the cell,[8] mitochondria dynamically modulate many other fundamental cellular processes, including stem cell self-renewal and differentiation.[9–15] Mitochondrial dysfunction has been documented in many human disorders, including respiratory diseases such as chronic obstructive pulmonary disease (COPD), asthma,

and idiopathic pulmonary fibrosis.[16–19] Recent studies in the lung revealed that disruption of mitochondria-mediated calcium homeostasis, specifically in alveolar type 2 cells (AT2s), altered surfactant secretion and cell differentiation after bacterial infection.[20,21] Shortly after birth, decreased mitochondria abundance and altered mitochondria subcellular localization in AT2s impaired platelet-derived growth factor (PDGF) signaling from these cells.[22] During embryonic development, genetic inactivation of electron transport chain (ETC) complex I subunit *Ndufs2* impaired AT2-to-AT1 cell differentiation.[23] If and how diverse cell types respond differently to disruption of mitochondrial activity remains poorly understood. Given the complex cellular composition and the cardinal role as the frontline barrier against inhaled pathogens, the conducting airway epithelium serves as a rich setting to explore mitochondria-dependent cell behaviors.
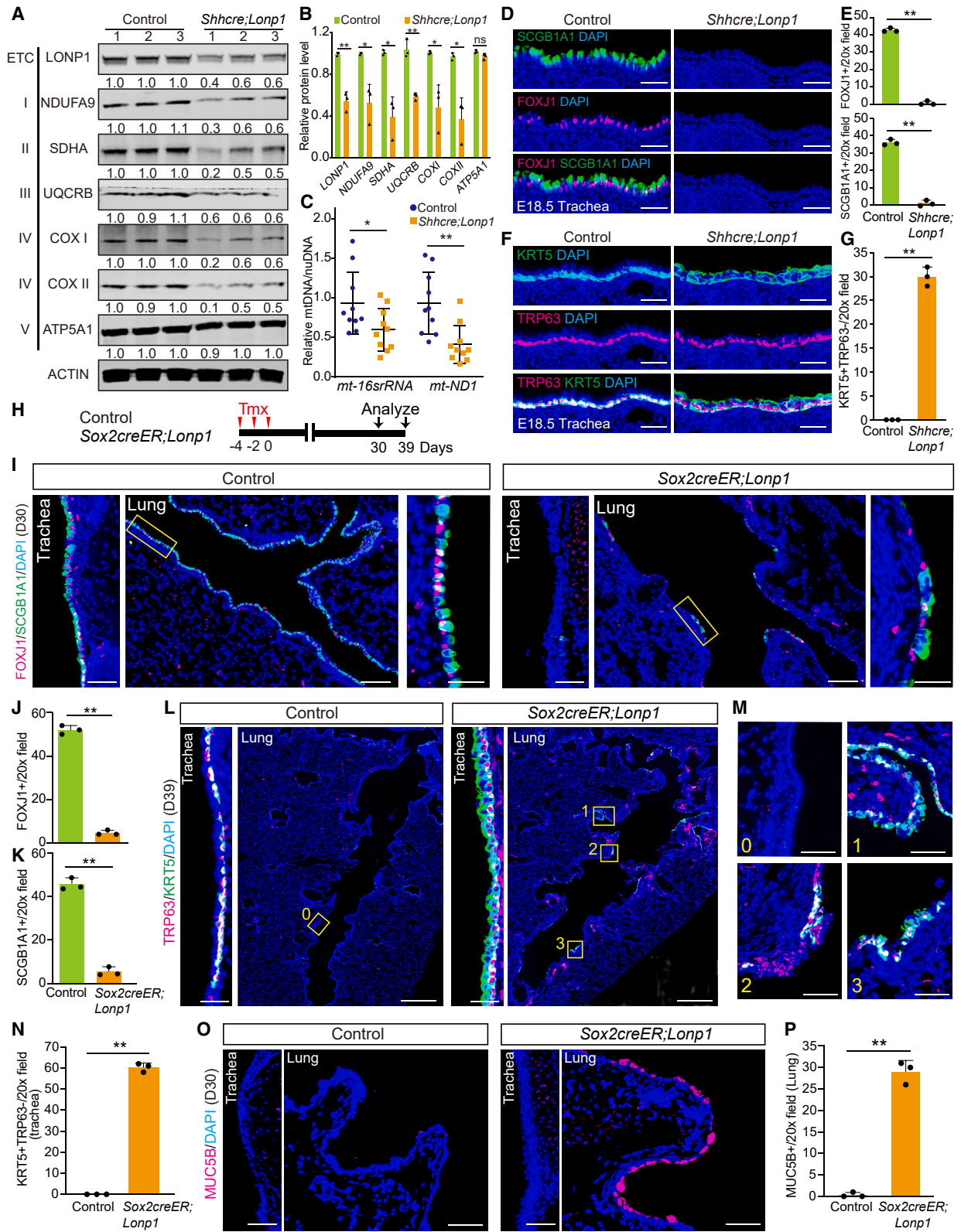
Figure 1. *Lonp1* is required for airway epithelial cell differentiation and homeostasis
(A and B) Western blot and quantification of ETC components in E13.5 lungs. *n* = 3 for each.
(C) Quantification of mitochondrial DNA copy number in E13.5 lungs. *n* = 10 for each.

(legend continued on next page)

Cell Stem Cell
Article

CellPress

Precise synthesis, folding, and assembly of proteins in mitochondria are essential for their health and function. Mitochondrial protein quality is closely monitored by a group of resident proteases that are specialized to degrade unfolded, misfolded, or damaged proteins.[24] AAA+ Lon protease 1 (LONP1) is a serine peptidase that is evolutionarily conserved from bacteria to human. In eukaryotes, LONP1 homo-oligomerizes to form a soluble hexameric ring in the mitochondrial matrix,[25,26] where it binds and cleaves a broad range of substrates.[27–35] In addition, LONP1 was found to possess protease-independent chaperone activity for protein stabilization,[36] as well as DNA binding activity for mitochondrial DNA maintenance.[37–39] Consistent with its multifaceted roles in maintaining mitochondrial health, a decrease in *LONP1* transcripts and genetic mutations in the gene are associated with multiple human diseases.[40,41] For example, mutations in *LONP1* were repeatedly found in patients with congenital diaphragmatic hernia (CDH), and we showed that inactivation of *Lonp1* in mice led to severe lung hypoplasia, recapitulating a key pathological feature of CDH.[42]

Respiratory distress is a leading cause of CDH infant death. Work from us and others shows that multiple CDH genes play essential roles in lung development, suggesting lung-intrinsic requirements for these genes.[43–45] To dissect the mechanism of *Lonp1* function in lung, here we conditionally inactivated *Lonp1* by using multiple cre lines targeting different cell types in lung. We show that inactivation of *Lonp1* in different cell types at different stages led to distinct phenotypes, suggesting that LONP1 plays an array of essential roles in controlling airway epithelial progenitor versus progeny cell composition and behavior in a context-dependent manner.

RESULTS

Lonp1 is required for balancing progenitor and progeny composition in the airway epithelium

Analysis of published single-cell RNA sequencing (scRNA-seq) showed that *Lonp1* is ubiquitously expressed in all developing and adult lung cell types, including epithelial, mesenchymal, endothelial, and immune cells, consistent with its general role in maintaining mitochondrial health[46,47] (Figure S1A). Widespread expression in the airway epithelium is validated by RNA-scope co-detection of *Lonp1* RNA with marker proteins for club, ciliated, and basal cells (Figure S1B). To investigate the requirements for *Lonp1* in lung, we inactivated *Lonp1* in the developing epithelium by generating *Shh^cre/+;Lonp1^flox/flox* (hereafter *Shhcre;Lonp1*) mutant mice (Figure S1C) and in the adult airway epithelium by generating *Sox2^creERT2/+;Lonp1^flox/flox* (hereafter *Sox2creER;Lonp1*) mutant mice (Figure 1H).

To determine how loss of *Lonp1* impacts mitochondrial function in the lung, we investigated multiple key mitochondrial parameters, including protein levels of ETC subunits, mitochondrial DNA copy numbers, generation of reactive oxygen species (ROS), protein solubility in the presence of detergent, and the oxygen consumption rate (OCR). By western blot using whole lung extracts at embryonic day (E) 13.5, we found that ETC components from complexes I–IV were significantly decreased in the *Shhcre;Lonp1* mutant lungs (Figures 1A and 1B). The extents of some of these decreases were even more so than the decrease in LONP1, possibly due to different rate of turnover in the cell or different proportional levels in the epithelium compared with the remainder of the lung. Interestingly, level of the nuclear-encoded subunit ATP5A1 (complex V) remained unchanged in the mutant. Similar changes were also reported when *Lonp1* is inactivated in the cardiomyocytes of heart tissue.[48,49]

Mitochondria are the major source of cellular ROS, which are primarily generated by the reduction of oxygen and leaked electrons from the ETC during oxidative phosphorylation. We quantified mitochondrial ROS from isolated epithelial cells using MitoSOX staining followed by flow cytometry[50] and found increased MitoSOX signal in the E13.5 *Shhcre;Lonp1* mutant lungs compared with control, consistent with increased ROS as a result of disrupted ETC (Figure S1D). We also found that the detergent-insoluble fractions of mitochondrial proteins, but not the soluble or total protein fractions, were more enriched in E13.5 *Shhcre;Lonp1* mutant lungs compared with control (Figure S1F), in line with previous findings that inhibition of LONP1 activity led to accumulation of protein aggregates.[33,35] Furthermore, we carried out seahorse mitochondria stress tests, which demonstrated a significant reduction of both basal and coupled mitochondrial respiration in sorted airway epithelial cells of *Lonp1* adult mutant compared with control (Figure S1E). Using quantitative PCR, we additionally found a significant reduction of mitochondrial DNA copy number in E13.5 *Shhcre;Lonp1* mutant lungs compared with control (Figure 1C). These results together suggest that *Lonp1* is essential for maintaining mitochondrial proteostasis and mitochondrial health in lung.

Shhcre;Lonp1 mutants died at birth, mimicking CDH patients.[42] Mutant mouse lungs show severe growth and branching morphogenesis defects that were evident at E13.5, suggesting that *Lonp1* is essential for normal lung development (Figures S1G and S1H). We found no change in apoptosis marker-cleaved caspase-3 staining (Figures S1I and S1J). By contrast, there is a significant loss of cell proliferation that is specific to the epithelium as indicated by reduced EdU labeling (Figures S1K and S1L). Consistent with this, there is a significant increase in cell cycle negative regulator CDKN1A protein (also termed P21) by staining (Figures S1M and S1N). These data suggest that reduced cell proliferation is likely a primary mechanism for the growth defect.

To investigate if *Lonp1* is required for cell differentiation, we examined major epithelial cell type markers in *Shhcre;Lonp1* airways compared with controls. At E16.5, while the alveolar type 1

(D–G) Immunostaining and quantification of club, ciliated, and basal cells (quantification of luminal KRT5) in E18.5 trachea. *n* = 3 for each. Scale bars, 50 μm.

(H) Experimental scheme for adult inactivation of *Lonp1*.

(I–P) Immunostaining and quantification of club, ciliated, basal (quantification of luminal KRT5), and goblet cells at indicated days after the last dose of tamoxifen. Boxed regions are magnified on the right. *n* = 3 for each. Scale bars: 50 μm for trachea, 200 μm for lung, and 20 μm for magnified panels on the right in (I). Scale bars: 30 μm for trachea and 500 μm for lung in (L). Scale bars: 50 μm in (M) and (O).

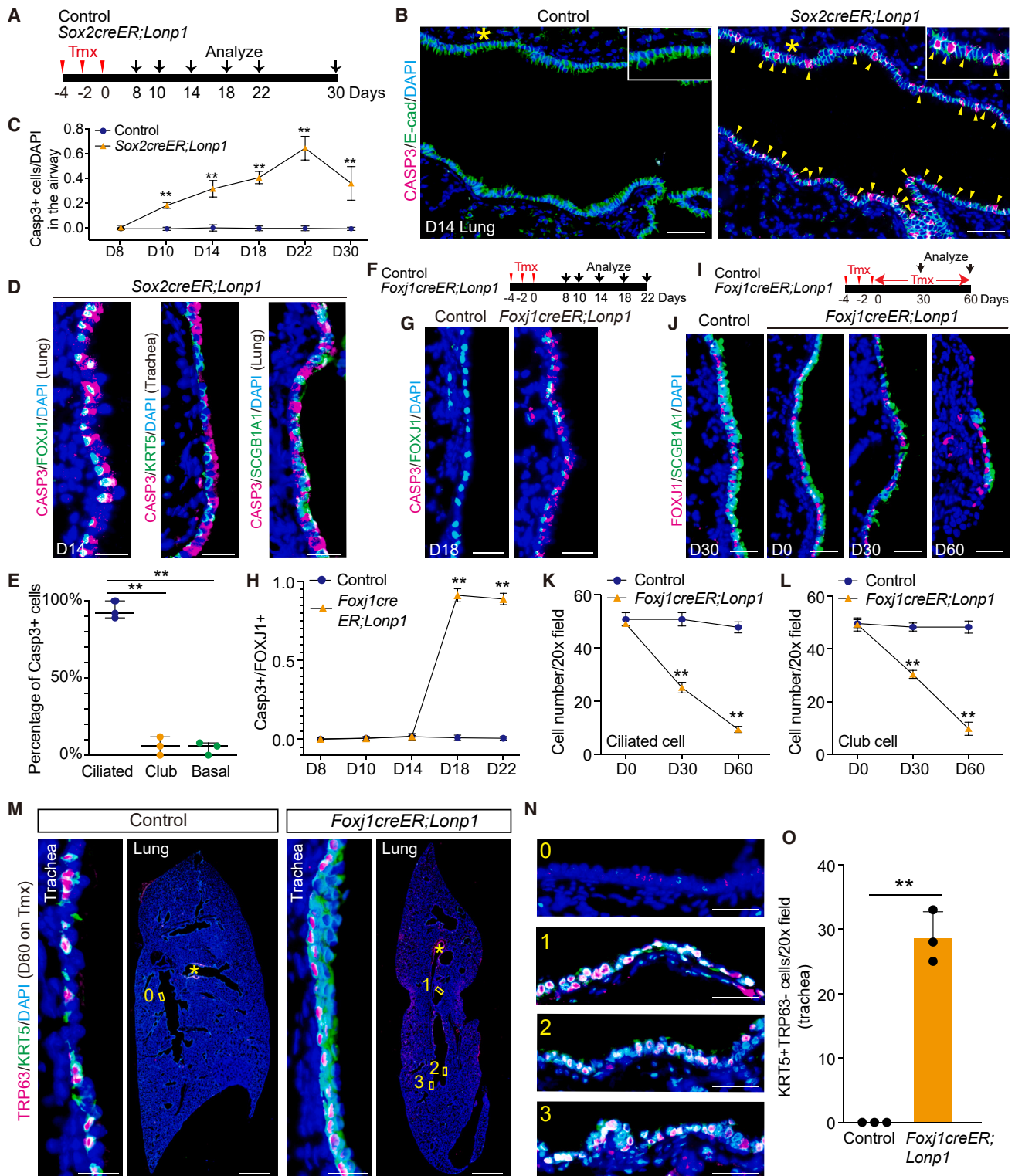Student's t test was used for (B), (C), (E), (G), (J), (K), (N), and (P).

See also Figure S1.

Figure 2. *Lonp1* is required cell-autonomously for ciliated cell survival

(A) Experimental scheme for analyzing apoptosis in *Sox2creER;Lonp1*.

(B and C) Immunostaining and quantification of cleaved caspase-3 for apoptotic cells (denoted by arrowheads) at day 14 post gene inactivation with quantification at multiple time points in (C). Regions marked by yellow asterisks were magnified in the upper inserts. Scale bars, 50 μm.

(D and E) Immunostaining and quantification of cleaved caspase-3 with ciliated, club, and basal cells at day 14 post gene inactivation. *n* = 3 for each. Scale bars, 30 μm.

Cell Stem Cell
Article

CellPress

and type 2 cell markers remain present (Figures S1O and S1P), there is a near complete loss of both club (SCGB1A1, SCGB3A2) and ciliated cell (FOXJ1) markers in the entire mutant epithelium at E18.5 (Figures 1D, 1E, S1Q, and S1R). Focusing on airway progenitor cells, while TRP63+KRT5+ basal cells were found on the basal side of the tracheal epithelium, similar to control, there is an ectopic emergence of TRP63-KRT5+ cells, constituting a majority of the mutant airway luminal cells (Figures 1F and 1G). These luminal cells also express KRT17 and KRT13, genes present in subsets of basal cells (Figures S1T–S1X).[51] These luminal cells have already taken on basal characteristics at E15.5, the stage of basal cell specification (Figure S1S). Based on a recent study delineating the progression of airway cell differentiation during development,[52] these results suggest that in the absence of *Lonp1*, primordial airway progenitor cannot differentiate into club and ciliated cells and instead differentiate into TRP63-KRT5+KRT13+KRT17+ luminal cells.

Altered airway progenitor/progeny composition was also observed in the *Sox2creER;Lonp1* adult mutants, including a clear reduction of club and ciliated cells (Figures 1I–1K) and an increase of TRP63-KRT5+ cells in the luminal layer of the trachea (Figures 1L, 1N, S1Y, and S1Z). Furthermore, we found that a group of basal-like cells (TRP63+KRT5+ or TRP63+KRT5−) ectopically appeared in the intrapulmonary airway of *Sox2creER;Lonp1* mutants in various regions, some with multi-layered metaplastic characteristics (Figures 1L, 1M, and S1Y). Interestingly, goblet cells were significantly increased in the intrapulmonary airway but not in the trachea of the *Lonp1* mutant (Figures 1O and 1P). It is notable that the metaplastic basal and goblet cells observed in the *Lonp1* mutant airway recapitulate the hallmarks of COPD pathology.

Lonp1 is required for the survival of terminally differentiated ciliated cells

Given that airway epithelial cells are relatively quiescent during homeostasis,[53,54] It is therefore intriguing that a severe airway phenotype developed within 1 month following *Lonp1* inactivation in the *Sox2creER;Lonp1* mutants. To explain the mechanism of this increased cellular turnover, we found a clear increase of cleaved caspase-3 staining in the mutant epithelium compared with control, where minimal signal was observed across all examined time points (Figures 2A–2C). This increase in apoptosis was observed as early as day 10, peaked at day 22, and remained elevated during the emergence of ectopic basal cells at day 30 (Figure 2C). After co-staining with major airway cell type markers, apoptosis was exclusively found in ciliated cells but not in either basal or club cells (Figures 2D and 2E). Release of cytochrome c from permeabilized mitochondrial membrane into the cytosol is considered a key step of apoptosis.

We found that compared with ciliated cells in the control airway where cytochrome c remained colocalized with mitochondria, which are enriched in the apical region, cytochrome c was detected in non-apical regions of ciliated cells in mutant airway, away from the apically localized mitochondria (Figures S2A–S2C). Notably, in the *Sox2creER;Lonp1* mutant, cell cycle arrest marker CDKN1A was detected only in few airway epithelial cells in the mutant airway, similar to the control (Figures S2D and S2E).

In the adult airway, to address if *Lonp1* is required in progenitor club or basal cells, or the terminally differentiated ciliated cells for the phenotypes, we inactivated *Lonp1* in club cells in *Scgb1a1creERT2/+;Lonp1flox/flox* (hereafter *Scgb1a1creER;Lonp1*) mutants (Figure S2F), in basal cells in *Trp63creERT2/+;Lonp1flox/flox;RosatdTomato* (hereafter *Trp63creER;Lonp1;tdT*) mutants (Figure S2L), and in ciliated cells in *Foxj1creERT2/+;Lonp1flox/flox* (hereafter *Foxj1creER;Lonp1*) mutants (Figure 2F), respectively. Neither club nor basal cell mutants showed any baseline phenotypes, unlike that in *Sox2creER;Lonp1* mutants. We subjected these mutants to naphthalene-induced injury (275 mg/kg). At this dose, naphthalene is known to ablate club cells in the intrapulmonary airway and both club and ciliated cells in the trachea (Figures S2G and S2M).[55] During the regenerative process, *Lonp1*-deficient club cells in the *Scgb1a1creER;Lonp1* mutant intrapulmonary airways maintained a comparable potential for self-renewal as control, as demonstrated by the nuclear staining of proliferative marker KI67 (Figures S2H and S2I). At day 21 post injury, previously lost club cells were similarly restored in the mutant airway as in the control (Figures S2J and S2K). In the trachea of *Trp63creER;Lonp1;tdT* mutants, KRT5+ transient amplifying cells were similarly expanded to the luminal side of the injured airways at day 3 post injury (Figure S2N). By day 9 post injury, proper basal/club/ciliated cell composition was restored in both the mutant and control, likely from basal cells that were lineage-traced by tdTomato (Figures S2O–S2Q). We found no significant differences of cell numbers between control and mutant mice at any examined time points (Figures S2R and S2S). These data suggest that *Lonp1* is dispensable for either club or basal cells during airway reconstitution following injury. By contrast, in the ciliated cell mutant compared with the control, robust apoptotic signal was enriched in ciliated cells starting at day 18 following *Lonp1* inactivation at baseline (Figures 2G and 2H), suggesting that *Lonp1* is cell-autonomously required in ciliated cells for the maintenance of cell survival. Noticeably, the apoptotic signal appeared in different time points post tamoxifen administration in the *Lonp1* mutants driven by either *Foxj1creER* (day 18) or *Sox2creER* (day 10). This discordance may be caused by different cre efficiency.[56,57] Alternatively, it is possible that in the *Sox2creER;Lonp1* mutant airways, additional cell non-autonomous factors from surrounding mutant

(F) Experimental scheme for inactivating *Lonp1* in ciliated cells.
(G and H) Immunostaining and quantification of cleaved caspase-3 in ciliated cells at multiple time points. $n = 3$ for each. Scale bars, 30 μm.
(I) Experimental scheme for continuous tamoxifen administration in *Foxj1creER;Lonp1*.
(J–L) Immunostaining and quantification of club and ciliated cells at denoted time points. $n = 3$ for each. Scale bars, 30 μm.
(M–O) Immunostaining and quantification of basal cells at day 60 on tamoxifen. Boxed regions are magnified in (N). Asterisks denote non-specific staining underneath the airway. $n = 3$ for each. Scale bars: 25 μm for trachea, 1 mm for lung, and 50 μm for magnified images in (N).
Student's t test was used for (C), (H), (K), (L), and (O). One-way ANOVA test was used for (E).
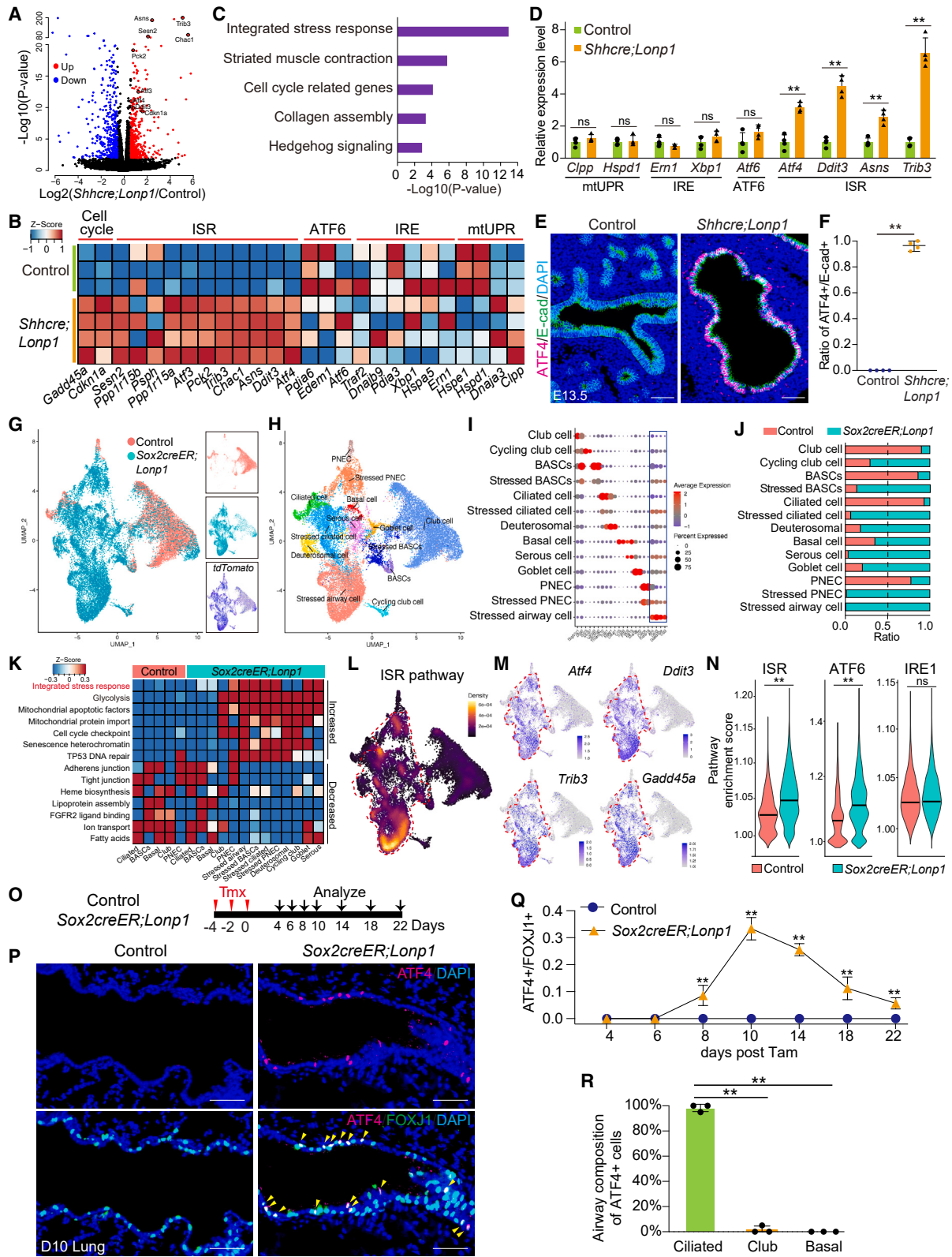See also Figure S2.

Figure 3. Transcriptomic analysis reveals the activation of ISR in airway epithelium of *Lonp1* mutants
(A) Volcano plot showing differentially expressed genes from bulk RNA-seq analysis. The ISR pathway genes were highlighted.
(B) Heatmap showing differential expression of cell stress- and cell cycle-related genes.

(legend continued on next page)

Cell Stem Cell
Article

CellPress

epithelial cells could function as pro-apoptotic signals, which synergized with factors in ciliated cells to accelerate their apoptotic process.

A previous study showed that airway cell type composition returned to normal after one-time genetic ablation of ciliated cells.[54] However, in *Sox2creER;Lonp1* mutant mice, every time a lost ciliated cell is replaced by a new one derived from progenitors such as club cells, it is already mutant for *Lonp1*, and it would be on the path to die. Such continuous ciliated cell death would cause a drain of progenitors in the *Sox2creER;Lonp1* mutant airways. To test this hypothesis, *Foxj1creER;Lonp1* mutants were subjected to repeated tamoxifen administration, leading to *Lonp1* recombination in nascent ciliated cells (Figure 2I). Aside from continued ciliated cell loss, there was also a significant decrease of club cells at day 30, progressing in severity at day 60, consistent with a continuous drain of progenitor club cells (Figures 2J–2L). Basal cell hyperplasia in the trachea and appearance of ectopic basal cells in the intrapulmonary airways were similarly found in the *Foxj1creER;Lonp1* mutant mice following repeated tamoxifen injections (Figures 2M–2O and S2T–S2W), even though at a lesser frequency compared with *Sox2creER;Lonp1* mutants. Taken together, these data suggest that despite similar imbalance of airway cell types found in the developing and adult *Lonp1* mutant airways, distinct cellular mechanisms are at play.

Transcriptome profiling revealed activation of ISR pathway in *Lonp1* mutant airways

To dissect the molecular changes leading to the *Lonp1* mutant phenotypes, we first performed bulk RNA-seq analysis using *Shhcre;Lonp1* and control lungs at E13.5. With cutoff at $p < 0.01$ and fold change > 1.5, 511 upregulated genes and 439 downregulated genes were identified in the mutant compared with control (Figure 3A). Among them are increased cell cycle negative regulator *Cdkn1a* and its direct target *Gadd45a* (Figure 3B), consistent with decreased cell proliferation described above. Aside from these, gene ontology analysis of differentially expressed genes revealed that integrated stress response (ISR), one of the three branches of endoplasmic reticulum (ER) stress responses, ranked at the top of enriched terms (Figure 3C). Activation of this stress pathway is highly selective, as neither IRE1 and ATF6 pathways, the other two branches of

ER stress response, nor the canonical mitochondrial stress pathway were affected in the *Lonp1* mutant (Figures 3B and 3D). We next validated ISR activation at the protein level by immunostaining of activating transcription factor 4 (ATF4), the key effector of the ISR pathway.[58] We found a clear increase of ATF4 in the nucleus of epithelial cells of *Lonp1* mutants (Figures 3E and 3F). Consistent with this, by immunostaining, phosphorylation of ATF4 upstream regulator eIF2α is increased in the *Lonp1* mutant lung (Figures S3A and S3B). Further upstream, as the principal kinase triggering the eIF2α-ATF4 cascade, phosphorylated PERK was significantly increased in the *Shhcre;Lonp1* mutant lungs compared with control (Figures S3C and S3D). These results demonstrate the activation of the PERK-eIF2α-ATF4 cascade in the *Lonp1* mutant airways compared with control.

In the adult mutant, to systematically profile the cellular heterogeneity and dissect the underlying molecular mechanisms, we carried out single-cell transcriptomic analysis of lineage-labeled epithelial cells sorted from *Sox2^{creERT2/+};Lonp1^{fl/fl};Rosa^{tdTomato}* mutant and control lungs at day 39 following *Lonp1* inactivation. A total of 27,402 epithelial cells (9,682 in control, 17,720 in mutant) passed quality control cutoffs and were used for further dimension reduction and integration. Unsupervised clustering and cell type identification using canonical marker genes from Lung CellCards[59] revealed the expected airway cell types in the control lung (Figures 3G–3I). In comparison in the mutant lung, club and ciliated cells were greatly reduced while basal and goblet cells were increased (Figures 3J and S3E), consistent with the results from immunostaining (Figures 1H–1P).

We note that for multiple cell type clusters, a portion of the mutant cells segregated away from equivalent control clusters (Figures 3G and 3H). Pathway enrichment analysis revealed that cell junctions and mitochondria-associated metabolic processes, such as heme and fatty acids biosynthesis, were reduced in the mutant cells (Figure 3K). Conversely, ISR, glycolysis, cell cycle checkpoint, and P53-mediated DNA repair were elevated in most of the mutant cell types (Figure 3K). Focusing in on the cell clusters that have shifted position in the mutant, even though they are characterized by the same cell type markers as their equivalent control cell type, these mutant cells show remarkably decreased expressions of marker genes and increased

(C) Top biological processes from GO analysis of differentially expressed genes.
(D) RT-qPCR quantification of stress-related genes at E13.5. $n = 4$ for each.
(E and F) ATF4 immunostaining and quantification with epithelium outlined by E-cadherin at E13.5. $n = 4$ for each. Scale bars, 50 μm.
(G) Integrated UMAP of control and *Sox2creER;Lonp1* adult lungs with individual conditions shown on the right. Feature plot of lineage reporter *tdTomato* shown on the lower right.
(H) UMAP with annotations of different cell types.
(I) Dot plot showing expression levels of identified marker genes.
(J) Ratio of control versus mutant cell numbers in each cell type.
(K) Heatmap showing Z scores of differentially enriched pathways.
(L) ISR pathway enrichment score projected onto UMAP. Red dashed lines outline mutant-specific clusters.
(M) Feature plots of core ISR genes.
(N) Violin plots showing enrichment scores for branches of the ER stress pathway.
(O) Experimental scheme for analyzing ISR activation in *Sox2creER;Lonp1*.
(P and Q) Immunostaining and quantification of ATF4 with FOXJ1 at denoted time points. Arrowheads denote ATF4+ ciliated cells. Scale bars, 50 μm.
(R) Quantifications of ATF4 co-staining with ciliated, club, and basal cell markers at day 10 post gene inactivation. $n = 3$ for each.
Student's t test was used for (D), (F), and (Q). Wilcox test was used for (N). One-way ANOVA test was used for (R).
See also Figure S3 and Table S2.

expressions of stress-responsive genes in the ISR pathway, such as *Atf4*, *Ddit3*, *Gadd45a*, and *Trib3* (Figure 3I). We therefore named them stressed ciliated cells, stressed PNECs, and stressed bronchioalveolar stem cells (BASCs). UMAP projection of enrichment score of the ISR pathway genes (Figure 3L), expression features of individual ISR marker genes (Figure 3M), as well as *in vivo* detections of *Atf4* RNA transcripts at 10 days post *Lonp1* inactivation (Figures S3F–S3H), revealed that ISR is broadly activated at the transcriptional level in the mutant airway epithelium.

Focusing on the ISR signature, highest on the spectrum is a mutant-specific cluster that we named stressed airway cells, which express minimum of the differentiated cell type marker genes (Figure 3I) but are nevertheless high-quality airway cells based on their expression of *Sox2*-lineage label tdTomato transcripts (Figure 3G insets). The presence of these cells was confirmed by immunostaining as E-cadherin+ airway epithelial cells without expression of major epithelial cell type markers (FOXJ1 for ciliated cells, SCGB1A1 for club cells, KRT5 for basal cells, and MUC5B for goblet cells) (Figure S3I). By single-cell trajectory pseudotime analysis using either club or basal progenitor cells as root cells, stressed airway cells were predicted at the end of the trajectory, immediately preceded by stressed ciliated cells (Figures S3J and S3K). Taken together, these data suggest that failure to maintain airway cell fate can be a long-term consequence of loss of *Lonp1*.

To confirm elevated ISR in the mutant, we assessed the presence of core ISR effector ATF4 at the protein level. In the *Sox2-creER;Lonp1* mutant airway but not in control, ATF4 protein was specifically detected in the nucleus of ciliated cells starting at day 8 (Figures 3O–3R). Nuclear ATF4 was not detected in other airway cell types, despite broader detection of its RNA signals in the scRNA-seq, suggesting cell-type-specific regulation of ATF4 at the post-transcriptional level, consistent with prior knowledge.[60] Nuclear ATF4 proteins peak at day 10 and declined to near baseline level by day 22 and thereafter, despite persistently elevated transcripts at day 39 in the scRNA-seq data, suggesting temporal-dynamic post-transcriptional regulation (Figure 3Q). Intriguingly, our scRNA-seq data revealed that in the *Lonp1*-deficient ciliated cells, there is a clear increase in the expression of the SCF ubiquitin ligase βTRCP (encoded by the gene *Btrc*), which is known to mediate ATF4 protein degradation, raising the possibility that this increase may further explain the discordance between the presence of *Atf4* transcripts and absence of ATF4 protein (Figure S3L).[61] For the other branches of the ER stress response, in the scRNA-seq data, the ATF6 branch genes also showed a statistically significant increase, while the IRE1 branch genes remained unchanged (Figures 3N and S3M). However, the N-terminal activated form of ATF6 was not detected in the nucleus of *Lonp1*-deficient epithelial cells across all time points examined, suggesting that the elevated transcripts do not translate into functional protein (Figure S3N).[62]

In the scRNA-seq dataset, basal cells were found in both control and mutant samples, expressing the same canonical markers, *Krt5* and *Trp63* (Figure S3O). To gain better resolution on the molecular features of the basal cells, bona fide basal cells with normalized expression value of *Krt5* > 0.5 or *Trp63* > 0.5 were selected for further subclustering analysis. Following unsupervised clustering, these basal cells were sepa-

rated into two clusters, annotated as basal-1 and basal-2, respectively (Figure S3P). Each cluster consists of cells originating from both the control and the *Lonp1* mutant (Figure S3Q). For basal-1, marker gene analysis revealed enrichment of Kruppel family members *Klf4*, *Klf6*, *Klf9*, and *Klf17*, AP-1 pathway genes *Fos* and *Jun*, and *Cav1* (Figures S3R and S3S). All of these factors have been reported to promote squamous cell commitment in stratified epithelium.[63–67] These characteristics of basal-1 cells resemble the molecular features of the basal cell subpopulation localized on the dorsal side of the trachea, which was shown to exhibit higher colony-forming capacity.[51,68] On the other hand, for basal-2, molecular features of club cells, including *Scgb1a1* and *Scgb3a1*, were relatively enriched in addition to their clear expression of basal markers, suggesting that these cells may be primed for transition to club cells (Figures S3R and S3S). Immunostaining experiments revealed that, in the *Sox2creER;Lonp1* mutant, KRT17 was ectopically detected in basal cells on the ventral side of the trachea, unlike their normal restriction to the dorsal side in the control trachea (Figures S3T and S3U). Noticeably, many of these basal cells in the mutant also express KRT13 (Figures S3V and S3W), a marker for squamous epithelium and "hillock" cells of high proliferative capacity in the trachea.[47,69,70] Furthermore, the ectopic basal cells found in the intrapulmonary airway of *Sox2creER;Lonp1* also express KRT17 (Figures S3X and S3Y). Taken together, our data suggest that *Lonp1*-deficient adult airways show significant transformation toward squamous basal cell and goblet cell characteristics, mimicking the composition of COPD airways.

Elevated ISR is responsible for airway phenotypes in the adult *Lonp1* mutants

The striking ISR signature raised the possibility that it could be responsible for the phenotypes in the *Sox2creER;Lonp1* mutant airway. To test this, we first explored if airway cell apoptosis can be inhibited by treatment using ISRIB, a small-molecule inhibitor of ISR (Figure S4A). The nuclear staining of ATF4 in the ciliated cells of *Sox2creER;Lonp1* mutant mice was significantly reduced in the presence of ISRIB (Figures S4B and S4C), suggesting that ISR activation was efficiently blocked by ISRIB in the mutant lung. This led to a striking reduction of apoptotic cells (Figures S4D and S4E), suggesting that ISR activation is the leading cause of ciliated cell death.

We also tested the requirement for *Atf4* genetically by conditionally inactivating *Atf4* in the *Lonp1* mutant background through generating *Sox2^{creERT2/+};Lonp1^{flox/flox};Atf4^{flox/flox}* (hereafter *Sox2creER;Lonp1;Atf4*) compound mutants (Figure 4A). Assay of cell death revealed that apoptosis was largely reversed by *Atf4* inactivation (Figures 4B and 4C). Moreover, the ectopic subcellular localization of cytochrome c in the *Lonp1*-deficient ciliated cells was also largely rescued (Figures S4F and S4G), as was the loss of ciliated and club cells and the increase of basal cells (Figures 4D–4H).

ATF4 is known to control apoptotic genes through co-binding with one of its direct transcriptional targets, DDIT3.[71,72] To address if DDIT3 is required for the *Lonp1* mutant phenotypes, we inactivated *Ddit3* in the *Lonp1* mutant background by generating *Sox2^{creERT2/+};Lonp1^{flox/flox};Ddit3^{flox/flox}* (hereafter *Sox2creER;Lonp1;Ddit3*) compound mutants (Figure 4I). Similar to
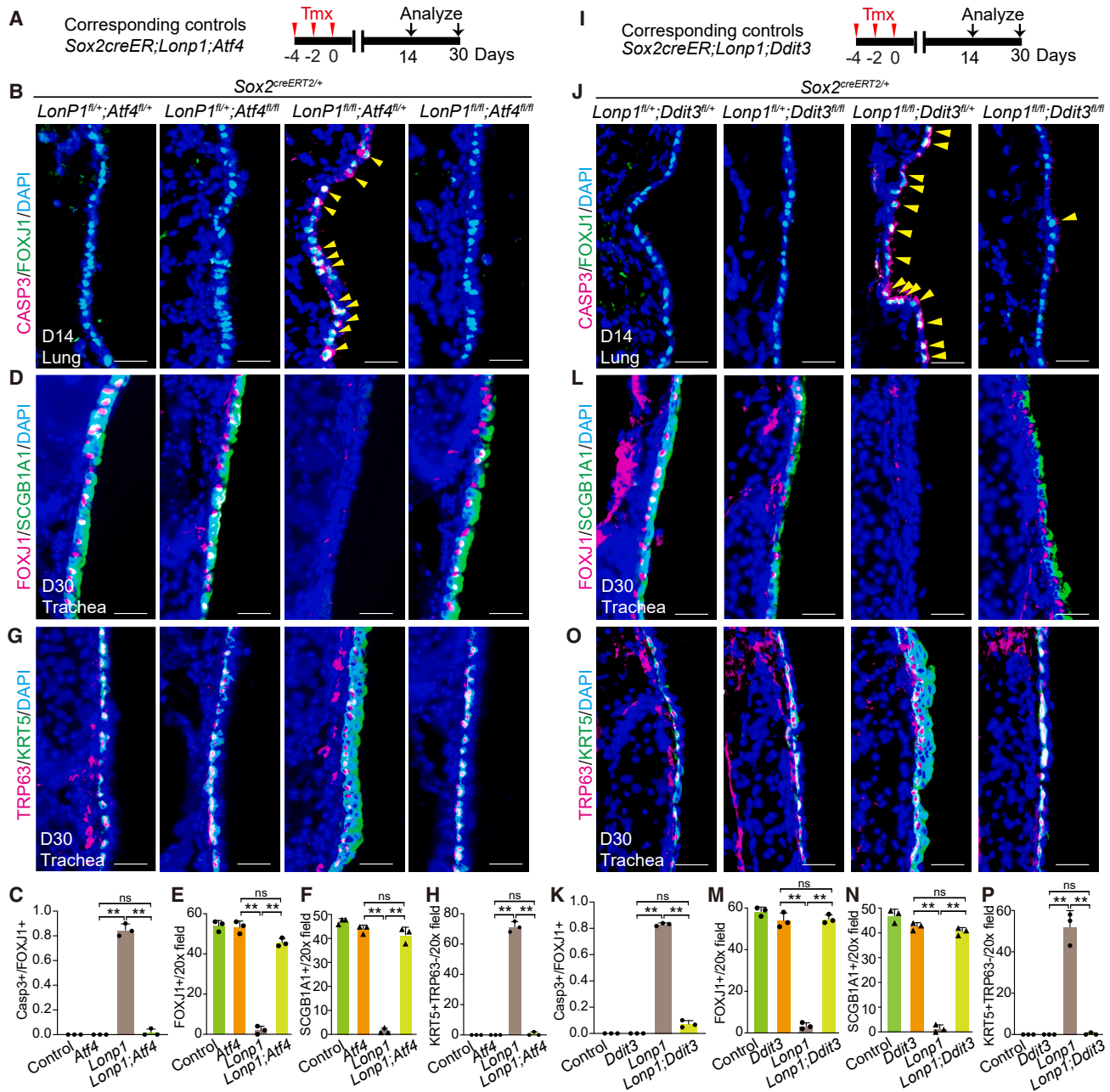
Figure 4. *Lonp1* maintains airway homeostasis through repressing ISR

(A and I) Experimental schemes for analyzing airway phenotypes in *Sox2creER;Lonp1;Atf4* (A) and *Sox2creER;Lonp1;Ddit3* (I).

(B–P) Immunostaining and quantification of proteins as labeled. Quantification of luminal KRT5+TRP63− cells is shown in (H) and (P). Arrowheads denote apoptotic ciliated cells. $n = 3$ for each. Scale bars, 30 μm.

One-way ANOVA test was used for (C), (E), (F), (H), (K), (M), (N), and (P).

See also Figure S4.

Sox2creER;Lonp1;Atf4 mutants, ciliated cell apoptosis was largely rescued by *Ddit3* inactivation in the *Lonp1* mutant background (Figures 4J and 4K). The reduction of both ciliated and club cells and the increase of basal cells were also significantly reversed in the *Sox2creER;Lonp1;Ddit3* compound mutant (Figures 4L–4P). To ensure that these genetic rescues were not due to reduced cre-mediated recombination of individual alleles

in the compound mutants, we showed that a similar extent of *Lonp1* RNA reduction was achieved between single and double mutants (Figures S4H and S4I). These findings together suggest that elevated ISR pathway is responsible for loss of ciliated cells in the *Lonp1* adult mutant airway, leading to a cascade of airway phenotypes including the loss of club cells and ectopic increase of basal cells.
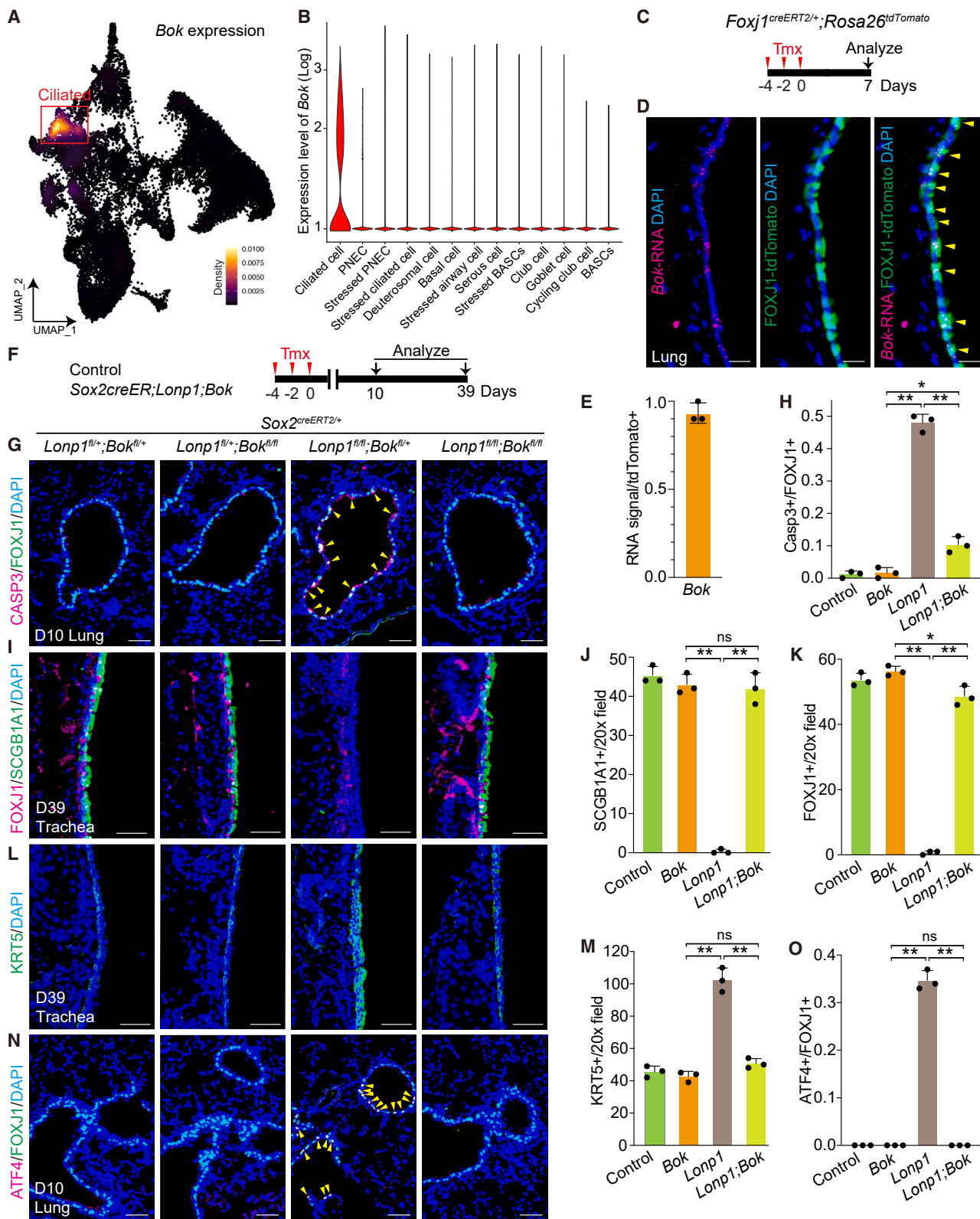
Figure 5. *Bok* expression in ciliated cells is required for ISR activation and apoptosis in *Lonp1* mutant

(A) Density plot showing *Bok* expression in the integrated UMAP.

(B) Violin plot showing *Bok* expression across cell types.

(legend continued on next page)

Cell Stem Cell
Article

CellPress

As elevated ATF4 was also observed in the *Shhcre;Lonp1* embryonic lung, we next determined if the branching defects of *Lonp1* mutant could be rescued by introducing *Atf4* flox alleles into the *Shhcre;Lonp1* background. Intriguingly, we found that inactivating *Atf4* in the developing lung using *Shhcre* led to drastic lung defects, including extremely hypoplastic trachea and lung lobes (Figure S4J). This striking phenotype remained in the *Shh^{cre/+};Lonp1^{f/f};Atf4^{f/f}* mutant background (Figure S4J). These data suggest an unexpected requirement for ISR in promoting early lung development. Such early phenotypes precluded us from addressing if elevated *Atf4* plays a role in mediating *Shhcre;Lonp1* phenotypes during lung development.

Bok expression in ciliated cells is required not only for apoptosis but also for increased ISR in the adult *Lonp1* mutant airway

To address the molecular basis leading to ciliated cell-specific death, we analyzed our scRNA-seq data for expression of both pro-apoptotic and pro-survival genes of the BCL-2 family, the central factors that control apoptosis[73–75] (Figure S5A). Among them, we noted that Bcl-2-related ovarian killer (BOK), a lesser known pro-apoptotic effector in BCL-2 family proteins,[76] is greatly enriched in ciliated cells in both normal and *Lonp1*-deficient airway epithelium (Figures 5A, 5B, S5B, and S5C). This expression specificity was further confirmed by analysis of published scRNA-seq data of the wild-type airway (Figures S5D and S5E). We validated this finding *in vivo* by RNAscope in *Foxj1^{creERT2/+};Rosa^{tdTomato}* lineage-labeled ciliated cells (Figures 5C–5E). Such specificity led us to hypothesize that BOK may function to mediate ISR-induced apoptosis in ciliated cells. To test this, we inactivated *Bok* in the *Lonp1* mutant background by generating *Sox2^{creERT2/+};Lonp1^{flox/flox};Bok^{flox/flox}* (hereafter *Sox2creER;Lonp1;Bok)* compound mutants (Figure 5F). Caspase-3 and cytochrome c staining revealed that apoptosis resulting from loss of *Lonp1* was largely reversed by *Bok* inactivation (Figures 5G, 5H, S5F, and S5G). So was the loss of club and ciliated cells and the increase of basal cells (Figures 5I–5M). In cell culture, it has been shown that BOK can also function upstream to control ATF4 expression.[77] Consistent with this, we found that the ectopic activation of ATF4 in the airway of *Lonp1* single mutant was fully reversed by additional knockout of *Bok* (Figures 5N and 5O). Taken together, our data indicate that BOK functions downstream of LONP1 to control ISR-induced cell death in ciliated cells.

Lonp1 promotes pathologic basal progenitor cell migration through repressing ISR following influenza infection

It has been shown that KRT5+ basal cells are induced in the lung airway post influenza infection and migrate into the injured alveoli with the capability to give rise to distinct progeny cell types.[5,6,78]

To investigate if LONP1 plays a role in mediating such injury response, we inactivated *Lonp1* in airway stem cells while performing lineage tracing by using *Sox2^{creERT2/+};Lonp1^{fl/fl}; Rosa^{tdTomato}* (hereafter *Sox2creER;Lonp1;tdT)* (Figure 6A).[57,79] At 14 days post viral infection, we found a similar number of airway KRT5+ cells in the *Lonp1* mutant compared with control (Figures 6B and 6C), suggesting that the ability of airway progenitors to give rise to these cells is not affected. Interestingly, unlike in the control, where the airway-derived KRT5+ basal cells migrated into the damaged alveolar region and formed KRT5+ "pods," they were rarely seen in the damaged alveoli of *Sox2-creER;Lonp1;tdT* lungs (Figures 6B and 6D). This phenotype is unlikely a result of delayed migration, as the pathologic basal cells continued to be absent from damaged alveolar region at 54 days post injury (Figures S6A–S6C). We also addressed whether the reduced migration could be due to resistance to influenza infection in *Lonp1*-deficient mice by examining weight loss (Figure S6D) and viral load (Figure S6E) post viral infection. Instead of a decrease, our results show increased weight loss and virus persistence in the *Sox2creER;Lonp1* mutant, suggesting that reduced KRT5+ pod cell migration is not due to a decrease in the severity of injury in the mutant. Collectively, these *in vivo* data suggest that *Lonp1* is required for KRT5+ pod cell migration following influenza infection.

The lack of migration phenotype in the *Lonp1* mutant is of interest also because current knowledge on the molecular control of KRT5+ pods migration remains limited.[79,80] Immunostaining revealed that post influenza infection, ATF4 is highly expressed in the nucleus of KRT5+ cells in the airways of *Sox2creER; Lonp1;tdT* but not in control mice (Figures 6E and 6F). While no evidence of apoptosis was observed (Figure 6G), one of the ISR downstream factor CDKN1A was found upregulated in the basal cells of the mutants (Figures 6H and 6I). To determine if elevated ISR may be responsible for the failure of KRT5+ cell migration, we carried out influenza infection in aforementioned *Sox2creER;Lonp1;Atf4* compound mutants *and Sox2creER; Lonp1;Atf4*/+ single mutants as controls (Figure 6J). Interestingly, KRT5+ pods returned in the damaged alveoli of the compound mutants (Figures 6K–6M). These findings demonstrate that loss of *Lonp1* led to elevated ISR, which in turn suppress KRT5+ cell migration into the alveolar region following injury.

Bok is required for ISR activation in stalled airway basal progenitor cells in *Lonp1* mutants following influenza infection

Given that *Bok* is required for ISR activation in the ciliated cells, we wondered if *Bok* would also play a role in stalled basal cells of *Lonp1* mutants after flu infection. To determine whether *Bok* is expressed in the influenza-injured airway epithelium, we performed scRNA-seq using control and injured lungs following influenza infection at the start of ectopic airway basal cell

---

(C) Experimental scheme for analyzing *Bok* expression in *Foxj1creER;tdTomato*.

(D and E) RNAscope staining and quantification of *Bok* RNA with lineage reporter tdTomato. Arrowheads denote *Bok*-expressing ciliated cells. $n = 3$. Scale bars, 20 μm.

(F) Experimental scheme for analyzing airway phenotypes in *Sox2creER;Lonp1;Bok*.

(G–O) Immunostaining and quantification of proteins as labeled. Arrowheads denote co-staining. $n = 3$ for each. Scale bars, 50 μm.

One-way ANOVA test was used for (H), (J), (K), (M), and (O).

See also Figure S5.

Cell Stem Cell
Article

🗘 **CellPress**
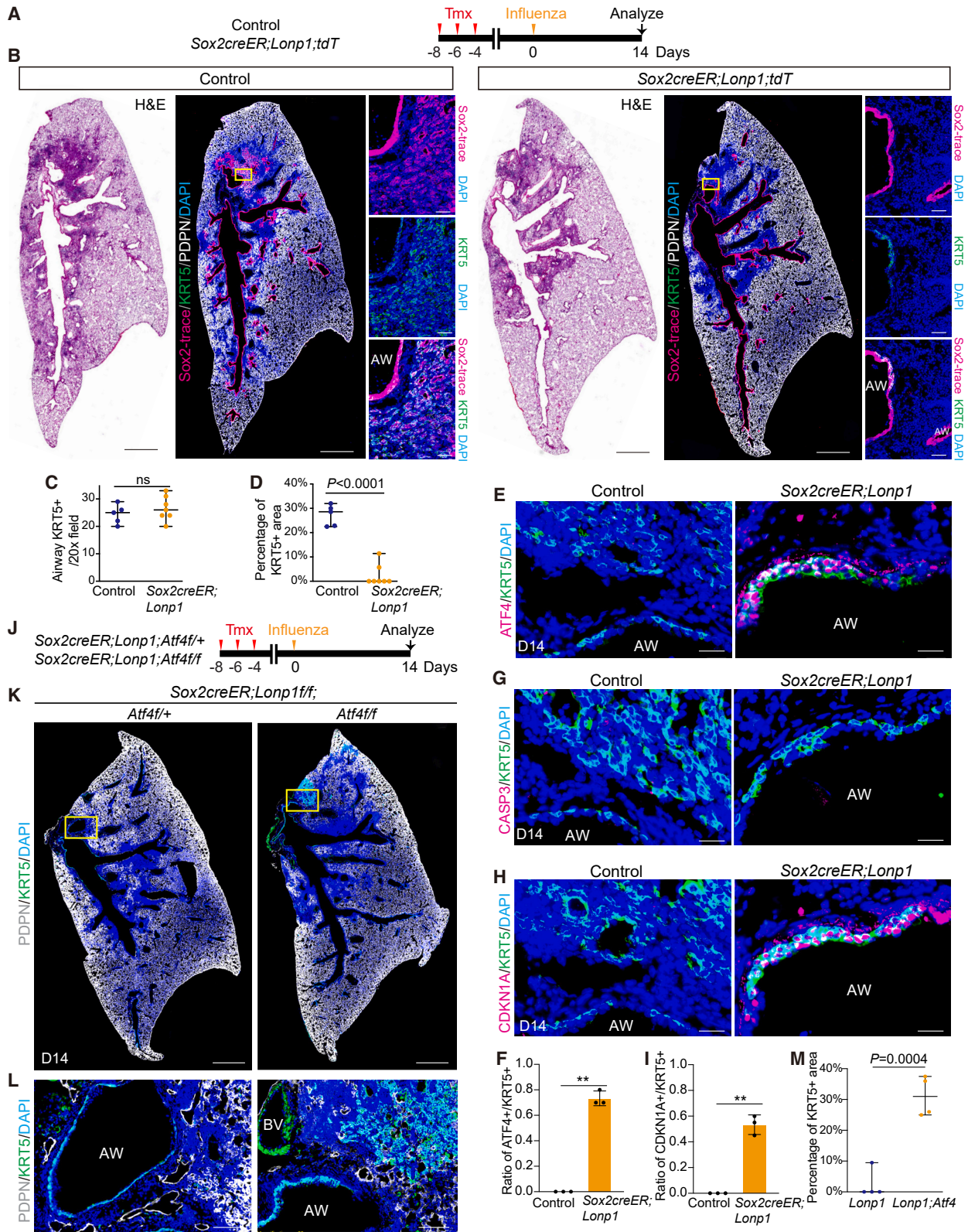
migration (day, day 11), as well as post migration (day 20) (Figure 7A). Unsupervised clustering showed that two separated populations (I and II) of KRT5+ cells appeared *de novo* after flu infection (Figures 7B, 7C, and S7A). Population I was mainly composed of cells from day 11, while population II was composed of cells from both day 11 and day 20 (Figures S7B and S7C). Marker gene analysis revealed that ectopic basal cells in population I express proliferating genes including *Mki67*, *Birc5*, and *Top2a*. In comparison, cells in population II express multiple genes associated with cell migratory processes, such as *Alcam*, *Runx1*, and *Krt15*[81–85] (Figures 7C, 7D, and S7A). *Trp63*, recently reported to be responsible for regulating basal cell migration,[80] was also found upregulated in population II (Figures 7C and 7D). These data align well with the dynamics that ectopic basal cells undergo proliferation in the airways between 7–11 days post flu infection and migrate into damaged alveoli thereafter.[6,57]

Through differentially expressed gene analysis, we found that *Bok* was highly enriched in the proliferating ectopic basal cells (Figures 7D and 7E). RNAscope assay showed that *Bok* transcripts were preferentially detected in the ectopic basal cells residing along the airway, compared with those that have migrated into the alveolar regions (Figures 7F and 7G). This *Bok* expression pattern led us to hypothesize that it may play a role in the activation of ISR in *Lonp1*-deficient pathologic basal cells and their migration. To test this, we performed influenza infection in the lungs of *Sox2creER;Lonp1;Bok* compound mutants and *Lonp1* single mutants (*Sox2creER;Lonp1;Bok/+*) and compared the migration of KRT5+ cells into the alveolar region (Figure 7H). We found that the stalled airway basal cells in the *Lonp1* single mutants after flu injury regained their migratory capacity in the compound mutants and colonized in the damaged alveoli after flu injury (Figures 7I–7K). Immunostaining showed that activation of ATF4 and the resulting increase of senescence-associated factor CDKN1A in the stalled basal cells of *Lonp1* mutants were significantly diminished in the compound mutants (Figures S7D–S7G). These *in vivo* findings suggest that *Bok* expression predisposes airway ectopic basal cells to be sensitive to ISR in the absence of *Lonp1*-mediated mitochondrial homeostasis.

LONP1 is reduced in squamous airway epithelium of COPD lungs

The cellular phenotypes in the airway of adult *Lonp1* mutants recapitulate the common features of COPD airways, including ciliated and club cell loss, squamous basal cell metaplasia,

and goblet cell hyperplasia.[86] To address if *LONP1* could play a conserved role in the human lung during COPD pathogenesis, we assessed its expression levels in the lungs of normal and COPD donors. Published data[87] suggest that at the transcript level, there is no change of *LONP1* RNA expression in the airway epithelial cells of COPD compared with control (Figure S7H). Consistently, by antibody staining, similar protein levels of LONP1 were detected between control and non- or low-grade-squamous epithelium of COPD airways (Figures 7L and 7N). However, in high-grade-squamous epithelium, where basal cells are greatly increased in number and stratified (Figure 7M), we found a significant reduction of LONP1 protein staining intensity in samples from multiple patients (Figures 7L and 7N). Consistent with the apoptotic phenotype of the adult *Lonp1* mutant mice, apoptosis was detected in ciliated cells in the COPD airway (Figures S7I and S7J). Such downregulation of LONP1 protein in the human airway epithelium is consistent with a potential role in the pathogenesis of COPD.

DISCUSSION

While the roles of mitochondrial have been investigated in many cell types, there is limited direct *in vivo* comparison of mitochondria functional thresholds across progenitor and progeny cells. Inactivation of *Lonp1* simultaneously in multiple cell types presented a unique opportunity to determine how diverse cell types respond to the same level of mitochondrial deficiency. Our *in vivo* results demonstrate that, depending on context, disruption of mitochondrial activity could affect the behavior of either progenitor cells or terminally differentiated progeny cells; it could affect either cell proliferation, differentiation, survival, cell fate maintenance, or migration.

The phenotypes of the *Lonp1* mutant are informative not only for what cell types are absent but also for what ectopic cell types that emerged when mitochondrial threshold was lowered. These findings led us to propose a cellular energy landscape that is inspired by the Waddington landscape widely used to depict epigenomic states. In this cellular energy landscape (Figure 7O), certain early developmental events, such as primordial airway progenitor cell proliferation, demand over the threshold of energy supply in the *Lonp1* mutant and therefore cannot be executed. In comparison, the energy requirement for primordial progenitor differentiation into P63+Krt5+ basal cells is under the threshold and thereby occurred normally in the mutant. In the adult airway, the results that *Lonp1* is selectively required in ciliated cells are in line with the knowledge that the high-frequency

---

Figure 6. *Lonp1* promotes influenza-infection-induced pathologic basal progenitor cell migration through repressing ISR

(A) Experimental scheme for influenza infection.

(B) H&E analysis (left) and lineage tracing of SOX2+ airway progenitor cells (right) in virus-injured lungs. Boxed regions are magnified on the right to show that, compared with control, KRT5+ basal cells are stalled in the mutant airway. Scale bars, 1 mm for whole lung H&E and immunostaining. 50 μm for magnified images. AW, airway.

(C) Quantification of KRT5+ basal cells in injured airways. $n \geq 5$ for each.

(D) Quantification of damaged areas covered by KRT5+ basal cells. $n \geq 5$ for each.

(E–I) Immunostaining and quantification of proteins as labeled. $n = 3$ for each. Scale bars, 20 μm. AW, airway.

(J) Experimental scheme for influenza infection.

(K–M) Immunostaining of KRT5 and PDPN in virus-injured lungs. Boxed regions are magnified in (L). Percentage of damaged areas covered by KRT5+ basal cells is quantified in (M). $n = 4$ for each. Scale bars: 1 mm in (K) and 100 μm in (L).

Student's t test was used for (C), (D), (F), (I), and (M).

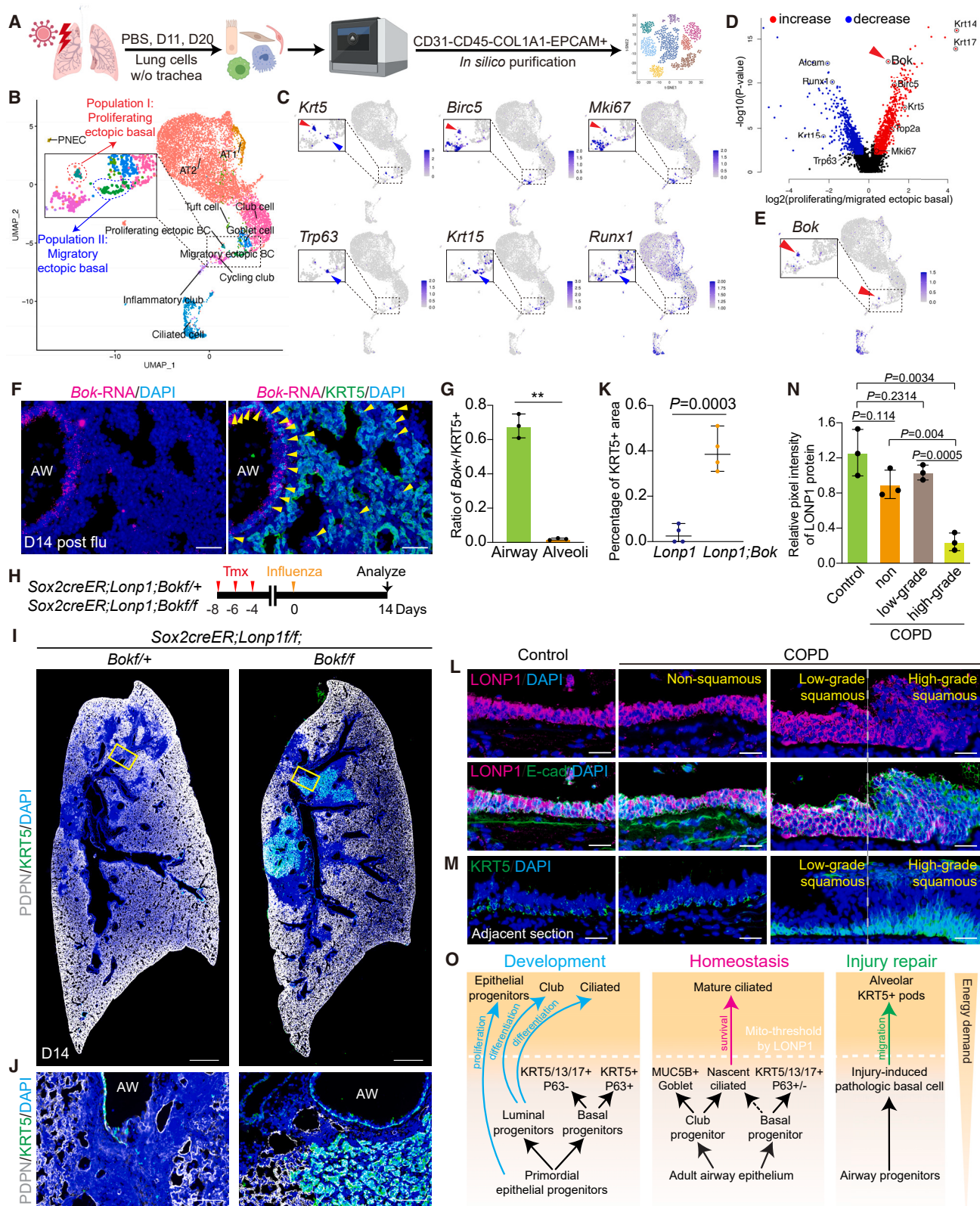See also Figure S6.

Figure 7. *Bok* is required for ISR activation and stalling of viral-infection-induced airway basal cells in *Lonp1* mutants

(A) Experimental scheme for scRNA-seq analysis of virus-injured lungs.

(B) Integrated UMAP of cells from PBS control, day 11 and day 20 post viral infection. Clusters of ectopic basal cells were magnified on the left.

(legend continued on next page)

Cell Stem Cell
Article

CellPress

beating of cilia relies on a considerable amount of ATP produced by mitochondria, which are localized adjacent to the basal bodies of the cilia.[88] In comparison to ciliated cells, ectopic cell types such as metaplastic basal cells and goblet cells appear less sensitive to mitochondrial perturbation, thereby having a selective advantage, and are allowed to emerge in the *Lonp1* mutant airway. The specific requirement for *Lonp1* shifts after injury, where airway-progenitor-derived KRT5+ cells elevated into a higher energy state after they delaminated from the airway heading into the alveolar region. Elucidation of other similar cellular energy landscapes within and outside of the lung could inform the hierarchy of cell types that are competitive to emerge under changing constraints of energy supply in either disease states or normal aging.

The findings that inactivation of *Lonp1* affected different cellular events in different settings suggest distinct downstream molecular mechanisms. In the two adult settings, elevated ATF4 led to differential cell behaviors. It has been shown that ATF4 can function acutely to relieve stress and secure cell survival, but chronically to trigger apoptosis.[60] ATF4 stability and transcriptional activity can be regulated by various post-translational modifications, including phosphorylation, acetylation, methylation, and ubiquitination.[61,89,90] Furthermore, ATF4 heterodimerization with different binding partners is associated with a switch between pro-survival versus pro-apoptotic outcomes.[71,91] In addition, various chromatin modifications on target genes are required for transcriptional regulation by ATF4.[92,93] We postulate that these context-dependent mechanisms, either alone or in combination, serve as key contributors to the distinct outcomes in the airway epithelium of *Lonp1* mutants.

To be able to predict which cell types are more sensitive than others to mitochondrial deficiency, we show that the selective presence of BOK may contribute to this specificity. BOK was identified as a pro-apoptotic BCL-2 family protein with restricted expression in reproductive tissues.[94] Recent studies show that BOK is required for ER stress-triggered apoptosis[77]; however, this role remains debated.[95,96] Our findings here show that in the adult airway, BOK is not only specifically expressed in ciliated cells but is also essential for ISR activation and apoptosis of these cells. In our model, BOK bridges the gap between mitochondrial proteostasis and ER stress signaling. This is further supported by data suggesting that BOK protein is localized at the mitochondria-associated ER membrane and regulates calcium flux between these organelles.[97]

Following influenza infection, while transcription factors, including HIF1α and TRP63, have been shown to play critical roles in rewiring the transcriptional programs of airway cells into basal pods and potentiate their migration,[79,80] molecular regulators of the process remain poorly understood. Here, our results suggest that compared with the formation of these ectopic basal cells, their migration is most sensitive to mitochondrial deficiency. In a normal airway, LONP1, acting to limit ISR, functions as a rheostat in airway progenitors to fine-tune their response to injury.

In summary, our findings here demonstrate that in a complex tissue, different progenitor or progeny cell types, as well as different cellular behaviors, present distinct sensitivity to impaired mitochondrial function. The presence of *Bok* could serve as a predictor for which cell types may be prone to cellular stress from mitochondria. Such context-dependent specificity informs how manipulating mitochondrial activity could be leveraged to promote healthy cell behavior and prevent disease in selected cell types.

Limitations of the study

Aside from targeting *Lonp1*, exploring other avenues to tune mitochondrial function would address how different thresholds impact different airway cell types. In humans, whether reduction of LONP1 or compromised mitochondrial function would trigger remodeling of the human airways could be explored using human iPSCs or primary cell-derived organoids.

STAR★METHODS

Detailed methods are provided in the online version of this paper and include the following:

- KEY RESOURCES TABLE
- RESOURCE AVAILABILITY
  - Lead contact
  - Materials availability
  - Data and code availability
- EXPERIMENTAL MODEL AND SUBJECT DETAILS
  - Mice
  - Human donors and tissue collection
- METHOD DETAILS
  - Tissue preparation and immunofluorescent staining
  - EdU analysis for cell proliferation
  - RNAscope
  - Mitochondrial DNA copy number analysis
  - Mitochondrial ROS measurement by MitoSOX
  - Mitochondrial OCR analysis

(C) Feature plots showing marker genes in proliferative (denoted by red arrowheads) and migratory (denoted by blue arrowheads) infection-induced basal cells.

(D) Volcano plot showing differentially expressed genes between proliferative and migratory ectopic basal cells. Arrowhead denotes *Bok*.

(E) Feature plot of *Bok* showing its preferential expression in proliferative ectopic basal cells (denoted by arrowhead).

(F and G) RNAscope staining and quantification of *Bok* expression at day 14 post viral infection. Arrowheads denote *Bok*-expressing basal cells. *n* = 3 for each. Scale bars, 50 μm.

(H) Experimental scheme for influenza infection.

(I–K) Immunostaining and quantification of KRT5 at day 14 post viral infection. Boxed regions are magnified in (J). *n* = 4 for each. Scale bars: 1 mm in (I) and 100 μm in (J).

(L and M) Immunostaining of LONP1 protein (L) and KRT5+ basal cells (M) in the adjacent sections of human control and COPD airways. Dashed line denotes low-grade to high-grade transition of squamous epithelium. Scale bars, 30 μm.

(N) Quantification of LONP1 protein levels in control and COPD airways. *n* = 3 for each.

(O) Cellular energy landscape of the airway epithelium.

Student's t test was used for (G) and (K). One-way ANOVA test was used for (N).

See also Figure S7 and Table S1.

- ○ Mitochondria isolation and protein fractionation
- ○ Quantitative PCR (qPCR)
- ○ Western blot analysis
- ○ Bulk RNA-seq and data analysis
- ○ Tissue dissociation and sorting of epithelial cells
- ○ Single-cell RNA-seq and data analysis
- ○ Pathway enrichment analysis
- ○ Influenza PR8 infection
- ● QUANTIFICATION AND STATISTICAL ANALYSIS

SUPPLEMENTAL INFORMATION

Supplemental information can be found online at https://doi.org/10.1016/j.stem.2024.08.001.

AUTHOR CONTRIBUTIONS

L.X. and X.S. designed experiments. L.X., C.T., J.B., R.M.E., and N.T. performed experiments. L.X. analyzed data. J.V., J.S.C., S.G., G.L., K.A., E.G., A.M., and L.E.C.A. procured human samples. D.J.M., Y.S., K.J.G., Z.B., and W.K.C. provided advice. L.X. and X.S. wrote the manuscript.

DECLARATION OF INTERESTS

The authors declare no competing interests.

REFERENCES

1. Cardoso, W.V., and Lü, J. (2006). Regulation of early lung morphogenesis: questions, facts and controversies. Development *133*, 1611–1624. https://doi.org/10.1242/dev.02310.

2. Tata, P.R., and Rajagopal, J. (2017). Plasticity in the lung: making and breaking cell identity. Development *144*, 755–766. https://doi.org/10.1242/dev.143784.

3. Hogan, B.L.M., Barkauskas, C.E., Chapman, H.A., Epstein, J.A., Jain, R., Hsia, C.C.W., Niklason, L., Calle, E., Le, A., Randell, S.H., et al. (2014). Repair and Regeneration of the Respiratory System: Complexity, Plasticity, and Mechanisms of Lung Stem Cell Function. Cell Stem Cell *15*, 123–138. https://doi.org/10.1016/j.stem.2014.07.012.

4. Basil, M.C., Alysandratos, K.D., Kotton, D.N., and Morrisey, E.E. (2024). Lung repair and regeneration: Advanced models and insights into human disease. Cell Stem Cell *31*, 439–454. https://doi.org/10.1016/j.stem.2024.02.009.

5. Kumar, P.A., Hu, Y., Yamamoto, Y., Hoe, N.B., Wei, T.S., Mu, D., Sun, Y., Joo, L.S., Dagher, R., Zielonka, E.M., et al. (2011). Distal airway stem cells yield alveoli in vitro and during lung regeneration following H1N1 influenza infection. Cell *147*, 525–538. https://doi.org/10.1016/j.cell.2011.10.001.

6. Vaughan, A.E., Brumwell, A.N., Xi, Y., Gotts, J.E., Brownfield, D.G., Treutlein, B., Tan, K., Tan, V., Liu, F.C., Looney, M.R., et al. (2015). Lineage-negative progenitors mobilize to regenerate lung epithelium after major injury. Nature *517*, 621–625. https://doi.org/10.1038/nature14112.

7. Kathiriya, J.J., Brumwell, A.N., Jackson, J.R., Tang, X., and Chapman, H.A. (2020). Distinct Airway Epithelial Stem Cells Hide among Club Cells but Mobilize to Promote Alveolar Regeneration. Cell Stem Cell *26*, 346–358.e4. https://doi.org/10.1016/j.stem.2019.12.014.

8. Kühlbrandt, W. (2015). Structure and function of mitochondrial membrane protein complexes. BMC Biol. *13*, 89. https://doi.org/10.1186/s12915-015-0201-x.

9. Spinelli, J.B., and Haigis, M.C. (2018). The multifaceted contributions of mitochondria to cellular metabolism. Nat. Cell Biol. *20*, 745–754. https://doi.org/10.1038/s41556-018-0124-1.

10. Murphy, M.P. (2009). How mitochondria produce reactive oxygen species. Biochem. J. *417*, 1–13. https://doi.org/10.1042/BJ20081386.

11. Giorgi, C., Marchi, S., and Pinton, P. (2018). The machineries, regulation and cellular functions of mitochondrial calcium (vol 19, pg 713, 2018). Nat. Rev. Mol. Cell Biol. *19*, 746. https://doi.org/10.1038/s41580-018-0066-2.

12. Wang, C.X., and Youle, R.J. (2009). The Role of Mitochondria in Apoptosis*. Annu. Rev. Genet. *43*, 95–118. https://doi.org/10.1146/annurev-genet-102108-134850.

13. Khacho, M., Clark, A., Svoboda, D.S., Azzi, J., MacLaurin, J.G., Meghaizel, C., Sesaki, H., Lagace, D.C., Germain, M., Harper, M.E., et al. (2016). Mitochondrial Dynamics Impacts Stem Cell Identity and Fate Decisions by Regulating a Nuclear Transcriptional Program. Cell Stem Cell *19*, 232–247. https://doi.org/10.1016/j.stem.2016.04.015.

14. Chakrabarty, R.P., and Chandel, N.S. (2021). Mitochondria as Signaling Organelles Control Mammalian Stem Cell Fate. Cell Stem Cell *28*, 394–408. https://doi.org/10.1016/j.stem.2021.02.011.

15. Yu, W.M., Liu, X., Shen, J., Jovanovic, O., Pohl, E.E., Gerson, S.L., Finkel, T., Broxmeyer, H.E., and Qu, C.K. (2013). Metabolic regulation by the mitochondrial phosphatase PTPMT1 is required for hematopoietic stem cell differentiation. Cell Stem Cell *12*, 62–74. https://doi.org/10.1016/j.stem.2012.11.022.

16. Mabalirajan, U., Dinda, A.K., Kumar, S., Roshan, R., Gupta, P., Sharma, S.K., and Ghosh, B. (2008). Mitochondrial structural changes and dysfunction are associated with experimental allergic asthma. J. Immunol. *181*, 3540–3548. https://doi.org/10.4049/jimmunol.181.5.3540.

17. Prakash, Y.S., Pabelick, C.M., and Sieck, G.C. (2017). Mitochondrial Dysfunction in Airway Disease. Chest *152*, 618–626. https://doi.org/10.1016/j.chest.2017.03.020.

18. Aghapour, M., Remels, A.H.V., Pouwels, S.D., Bruder, D., Hiemstra, P.S., Cloonan, S.M., and Heijink, I.H. (2020). Mitochondria: at the crossroads of regulating lung epithelial cell function in chronic obstructive pulmonary disease. Am. J. Physiol.-Lung Cell. Mol. Physiol. *318*, L149–L164. https://doi.org/10.1152/ajplung.00329.2019.

19. Spetz, J.K.E., Florido, M.H.C., Fraser, C.S., Qin, X., Choiniere, J., Yu, S.J., Singh, R., Friesen, M., Rubin, L.L., Salem, J.E., et al. (2022). Heightened apoptotic priming of vascular cells across tissues and life span predisposes them to cancer therapy-induced toxicities. Sci. Adv. *8*, eabn6579. https://doi.org/10.1126/sciadv.abn6579.

20. Islam, M.N., Gusarova, G.A., Das, S.R., Li, L., Monma, E., Anjaneyulu, M., Mthunzi, L., Quadri, S.K., Owusu-Ansah, E., Bhattacharya, S., and Bhattacharya, J. (2022). The mitochondrial calcium uniporter of pulmonary type 2 cells determines severity of acute lung injury. Nat. Commun. *13*, 5837. https://doi.org/10.1038/s41467-022-33543-y.

21. Ali, M., Zhang, X., LaCanna, R., Tomar, D., Elrod, J.W., and Tian, Y. (2022). MICU1-dependent mitochondrial calcium uptake regulates lung alveolar type 2 cell plasticity and lung regeneration. JCI Insight *7*, e154447. https://doi.org/10.1172/jci.insight.154447.

22. Zhang, K., Yao, E., Chen, B., Chuang, E., Wong, J., Seed, R.I., Nishimura, S.L., Wolters, P.J., and Chuang, P.T. (2022). Acquisition of cellular properties during alveolar formation requires differential activity and distribution of mitochondria. eLife *11*, e68598. https://doi.org/10.7554/eLife.68598.

Cell Stem Cell
Article

CellPress

23. Han, S., Lee, M., Shin, Y., Giovanni, R., Chakrabarty, R.P., Herrerias, M.M., Dada, L.A., Flozak, A.S., Reyfman, P.A., Khuder, B., et al. (2023). Mitochondrial integrated stress response controls lung epithelial cell fate. Nature 620, 890–897. https://doi.org/10.1038/s41586-023-06423-8.

24. Quirós, P.M., Langer, T., and López-Otín, C. (2015). New roles for mitochondrial proteases in health, ageing and disease. Nat. Rev. Mol. Cell Biol. 16, 345–359. https://doi.org/10.1038/nrm3984.

25. Shin, M., Watson, E.R., Song, A.S., Mindrebo, J.T., Novick, S.J., Griffin, P.R., Wiseman, R.L., and Lander, G.C. (2021). Structures of the human LONP1 protease reveal regulatory steps involved in protease activation. Nat. Commun. 12, 3239. https://doi.org/10.1038/s41467-021-23495-0.

26. Yang, J., Song, A.S., Wiseman, R.L., and Lander, G.C. (2022). Cryo-EM structure of hexameric yeast Lon protease (PIM1) highlights the importance of conserved structural elements. J. Biol. Chem. 298, 101694. https://doi.org/10.1016/j.jbc.2022.101694.

27. Bota, D.A., and Davies, K.J.A. (2002). Lon protease preferentially degrades oxidized mitochondrial aconitase by an ATP-stimulated mechanism. Nat. Cell Biol. 4, 674–680. https://doi.org/10.1038/ncb836.

28. Fukuda, R., Zhang, H., Kim, J.W., Shimoda, L., Dang, C.V., and Semenza, G.L. (2007). HIF-1 regulates cytochrome oxidase subunits to optimize efficiency of respiration in hypoxic cells. Cell 129, 111–122. https://doi.org/10.1016/j.cell.2007.01.047.

29. Granot, Z., Kobiler, O., Melamed-Book, N., Eimerl, S., Bahat, A., Lu, B., Braun, S., Maurizi, M.R., Suzuki, C.K., Oppenheim, A.B., and Orly, J. (2007). Turnover of mitochondrial steroidogenic acute regulatory (StAR) protein by Lon protease: the unexpected effect of proteasome inhibitors. Mol. Endocrinol. 21, 2164–2177. https://doi.org/10.1210/me.2005-0458.

30. Tian, Q., Li, T., Hou, W., Zheng, J., Schrum, L.W., and Bonkovsky, H.L. (2011). Lon peptidase 1 (LONP1)-dependent breakdown of mitochondrial 5-aminolevulinic acid synthase protein by heme in human liver cells. J. Biol. Chem. 286, 26424–26430. https://doi.org/10.1074/jbc.M110.215772.

31. Lu, B., Lee, J., Nie, X., Li, M., Morozov, Y.I., Venkatesh, S., Bogenhagen, D.F., Temiakov, D., and Suzuki, C.K. (2013). Phosphorylation of human TFAM in mitochondria impairs DNA binding and promotes degradation by the AAA+ Lon protease. Mol. Cell 49, 121–132. https://doi.org/10.1016/j.molcel.2012.10.023.

32. Matsushima, Y., Goto, Y., and Kaguni, L.S. (2010). Mitochondrial Lon protease regulates mitochondrial DNA copy number and transcription by selective degradation of mitochondrial transcription factor A (TFAM). Proc. Natl. Acad. Sci. USA 107, 18410–18415. https://doi.org/10.1073/pnas.1008924107.

33. Zurita Rendón, O., and Shoubridge, E.A. (2018). LONP1 Is Required for Maturation of a Subset of Mitochondrial Proteins, and Its Loss Elicits an Integrated Stress Response. Mol. Cell. Biol. 38, e00412-17. https://doi.org/10.1128/MCB.00412-17.

34. Silva-Pinheiro, P., Pardo-Hernández, C., Reyes, A., Tilokani, L., Mishra, A., Cerutti, R., Li, S., Rozsivalova, D.H., Valenzuela, S., Dogan, S.A., et al. (2021). DNA polymerase gamma mutations that impair holoenzyme stability cause catalytic subunit depletion. Nucleic Acids Res. 49, 5230–5248. https://doi.org/10.1093/nar/gkab282.

35. Ghosh, J.C., Seo, J.H., Agarwal, E., Wang, Y., Kossenkov, A.V., Tang, H.Y., Speicher, D.W., and Altieri, D.C. (2019). Akt phosphorylation of mitochondrial Lonp1 protease enables oxidative metabolism and advanced tumor traits. Oncogene 38, 6926–6939. https://doi.org/10.1038/s41388-019-0939-7.

36. Shin, C.S., Meng, S., Garbis, S.D., Moradian, A., Taylor, R.W., Sweredoski, M.J., Lomenick, B., and Chan, D.C. (2021). LONP1 and mtHSP70 cooperate to promote mitochondrial protein folding. Nat. Commun. 12, 265. https://doi.org/10.1038/s41467-020-20597-z.

37. Lu, B., Liu, T., Crosby, J.A., Thomas-Wohlever, J., Lee, I., and Suzuki, C.K. (2003). The ATP-dependent Lon protease of Mus musculus is a DNA-binding protein that is functionally conserved between yeast and mammals. Gene 306, 45–55. https://doi.org/10.1016/s0378-1119(03)00403-7.

38. Fu, G.K., and Markovitz, D.M. (1998). The human LON protease binds to mitochondrial promoters in a single-stranded, site-specific, strand-specific manner. Biochemistry 37, 1905–1909. https://doi.org/10.1021/bi970928c.

39. Chen, S.H., Suzuki, C.K., and Wu, S.H. (2008). Thermodynamic characterization of specific interactions between the human Lon protease and G-quartet DNA. Nucleic Acids Res. 36, 1273–1287. https://doi.org/10.1093/nar/gkm1140.

40. Sánchez-Lanzas, R., and Castaño, J.G. (2021). Mitochondrial LonP1 protease is implicated in the degradation of unstable Parkinson's disease-associated DJ-1/PARK 7 missense mutants. Sci. Rep. 11, 7320. https://doi.org/10.1038/s41598-021-86847-2.

41. Strauss, K.A., Jinks, R.N., Puffenberger, E.G., Venkatesh, S., Singh, K., Cheng, I., Mikita, N., Thilagavathi, J., Lee, J., Sarafianos, S., et al. (2015). CODAS syndrome is associated with mutations of LONP1, encoding mitochondrial AAA+ Lon protease. Am. J. Hum. Genet. 96, 121–135. https://doi.org/10.1016/j.ajhg.2014.12.003.

42. Qiao, L., Xu, L., Yu, L., Wynn, J., Hernan, R., Zhou, X., Farkouh-Karoleski, C., Krishnan, U.S., Khlevner, J., De, A., et al. (2021). Rare and de novo variants in 827 congenital diaphragmatic hernia probands implicate LONP1 as candidate risk gene. Am. J. Hum. Genet. 108, 1964–1980. https://doi.org/10.1016/j.ajhg.2021.08.011.

43. Stokes, G., Li, Z.W., Talaba, N., Genthe, W., Brix, M.B., Pham, B., Wienhold, M.D., Sandok, G., Hernan, R., Wynn, J., et al. (2024). Rescuing lung development through embryonic inhibition of histone acetylation. Sci. Transl. Med. 16, eadc8930. https://doi.org/10.1126/scitranslmed.adc8930.

44. McCulley, D.J., Wienhold, M.D., Hines, E.A., Hacker, T.A., Rogers, A., Pewowaruk, R.J., Zewdu, R., Chesler, N.C., Selleri, L., and Sun, X. (2018). PBX transcription factors drive pulmonary vascular adaptation to birth. J. Clin. Invest. 128, 655–667. https://doi.org/10.1172/JCI93395.

45. Domyan, E.T., Branchfield, K., Gibson, D.A., Naiche, L.A., Lewandoski, M., Tessier-Lavigne, M., Ma, L., and Sun, X. (2013). Roundabout receptors are critical for foregut separation from the body wall. Dev. Cell 24, 52–63. https://doi.org/10.1016/j.devcel.2012.11.018.

46. Zepp, J.A., Morley, M.P., Loebel, C., Kremp, M.M., Chaudhry, F.N., Basil, M.C., Leach, J.P., Liberti, D.C., Niethamer, T.K., Ying, Y., et al. (2021). Genomic, epigenomic, and biophysical cues controlling the emergence of the lung alveolus. Science 371, eabc3172. https://doi.org/10.1126/science.abc3172.

47. Montoro, D.T., Haber, A.L., Biton, M., Vinarsky, V., Lin, B., Birket, S.E., Yuan, F., Chen, S., Leung, H.M., Villoria, J., et al. (2018). A revised airway epithelial hierarchy includes CFTR-expressing ionocytes. Nature 560, 319–324. https://doi.org/10.1038/s41586-018-0393-7.

48. Li, Y., Huang, D., Jia, L., Shangguan, F., Gong, S., Lan, L., Song, Z., Xu, J., Yan, C., Chen, T., et al. (2023). LonP1 Links Mitochondria-ER Interaction to Regulate Heart Function. Research (Wash D. C) 6, 0175. https://doi.org/10.34133/research.0175.

49. Venkatesh, S., Li, M., Saito, T., Tong, M., Rashed, E., Mareedu, S., Zhai, P., Bárcena, C., López-Otín, C., Yehia, G., et al. (2019). Mitochondrial LonP1 protects cardiomyocytes from ischemia/reperfusion injury in vivo. J. Mol. Cell. Cardiol. 128, 38–50. https://doi.org/10.1016/j.yjmcc.2018.12.017.

50. Kauffman, M.E., Kauffman, M.K., Traore, K., Zhu, H., Trush, M.A., Jia, Z., and Li, Y.R. (2016). MitoSOX-Based Flow Cytometry for Detecting Mitochondrial ROS. React. Oxyg Species (Apex) 2, 361–370. https://doi.org/10.20455/ros.2016.865.

51. Zhou, Y.Z., Yang, Y., Guo, L.H., Qian, J., Ge, J., Sinner, D., Ding, H.X., Califano, A., and Cardoso, W.V. (2022). Airway basal cells show regionally distinct potential to undergo metaplastic differentiation. eLife 11, e80083. https://doi.org/10.7554/eLife.80083.

52. Kiyokawa, H., Yamaoka, A., Matsuoka, C., Tokuhara, T., Abe, T., and Morimoto, M. (2021). Airway basal stem cells reutilize the embryonic

proliferation regulator, Tgfbeta-Id2 axis, for tissue regeneration. Dev. Cell *56*, 1917–1929.e9. https://doi.org/10.1016/j.devcel.2021.05.016.

53. Rawlins, E.L., and Hogan, B.L.M. (2008). Ciliated epithelial cell lifespan in the mouse trachea and lung. Am. J. Physiol. Lung Cell. Mol. Physiol. *295*, L231–L234. https://doi.org/10.1152/ajplung.90209.2008.

54. Pardo-Saganta, A., Tata, P.R., Law, B.M., Saez, B., Chow, R.D.W., Prabhu, M., Gridley, T., and Rajagopal, J. (2015). Parent stem cells can serve as niches for their daughter cells. Nature *523*, 597–601. https://doi.org/10.1038/nature14553.

55. Hsu, H.S., Liu, C.C., Lin, J.H., Hsu, T.W., Su, K., and Hung, S.C. (2014). Repair of naphthalene-induced acute tracheal injury by basal cells depends on beta-catenin. J. Thorac. Cardiovasc. Surg. *148*, 322–332. https://doi.org/10.1016/j.jtcvs.2013.10.039.

56. Rawlins, E.L., Ostrowski, L.E., Randell, S.H., and Hogan, B.L.M. (2007). Lung development and repair: contribution of the ciliated lineage. Proc. Natl. Acad. Sci. USA *104*, 410–417. https://doi.org/10.1073/pnas.0610770104.

57. Ray, S., Chiba, N., Yao, C., Guan, X., McConnell, A.M., Brockway, B., Que, L., McQualter, J.L., and Stripp, B.R. (2016). Rare SOX2(+) Airway Progenitor Cells Generate KRT5(+) Cells that Repopulate Damaged Alveolar Parenchyma following Influenza Virus Infection. Stem Cell Rep. *7*, 817–825. https://doi.org/10.1016/j.stemcr.2016.09.010.

58. Pakos-Zebrucka, K., Koryga, I., Mnich, K., Ljujic, M., Samali, A., and Gorman, A.M. (2016). The integrated stress response. EMBO Rep. *17*, 1374–1395. https://doi.org/10.15252/embr.201642195.

59. Sun, X., Perl, A.K., Li, R., Bell, S.M., Sajti, E., Kalinichenko, V.V., Kalin, T.V., Misra, R.S., Deshmukh, H., Clair, G., et al. (2022). A census of the lung: CellCards from LungMAP. Dev. Cell *57*, 112–145.e2. https://doi.org/10.1016/j.devcel.2021.11.007.

60. Wortel, I.M.N., van der Meer, L.T., Kilberg, M.S., and van Leeuwen, F.N. (2017). Surviving Stress: Modulation of ATF4-Mediated Stress Responses in Normal and Malignant Cells. Trends Endocrinol. Metab. *28*, 794–806. https://doi.org/10.1016/j.tem.2017.07.003.

61. Lassot, I., Ségéral, E., Berlioz-Torrent, C., Durand, H., Groussin, L., Hai, T., Benarous, R., and Margottin-Goguet, F. (2001). ATF4 degradation relies on a phosphorylation-dependent interaction with the SCF(betaTrCP) ubiquitin ligase. Mol. Cell. Biol. *21*, 2192–2202. https://doi.org/10.1128/MCB.21.6.2192-2202.2001.

62. Ye, J., Rawson, R.B., Komuro, R., Chen, X., Davé, U.P., Prywes, R., Brown, M.S., and Goldstein, J.L. (2000). ER stress induces cleavage of membrane-bound ATF6 by the same proteases that process SREBPs. Mol. Cell *6*, 1355–1364. https://doi.org/10.1016/s1097-2765(00)00133-7.

63. Eckert, R.L., Adhikary, G., Young, C.A., Jans, R., Crish, J.F., Xu, W., and Rorke, E.A. (2013). AP1 transcription factors in epidermal differentiation and skin cancer. J. Skin Cancer *2013*, 537028. https://doi.org/10.1155/2013/537028.

64. Ding, X., Pan, H., Li, J., Zhong, Q., Chen, X., Dry, S.M., and Wang, C.Y. (2013). Epigenetic activation of AP1 promotes squamous cell carcinoma metastasis. Sci. Signal. *6*, ra28.21-13. S20–S15. https://doi.org/10.1126/scisignal.2003884.

65. Sastre-Perona, A., Hoang-Phou, S., Leitner, M.C., Okuniewska, M., Meehan, S., and Schober, M. (2019). De Novo PITX1 Expression Controls Bi-Stable Transcriptional Circuits to Govern Self-Renewal and Differentiation in Squamous Cell Carcinoma. Cell Stem Cell *24*, 390–404.e8. https://doi.org/10.1016/j.stem.2019.01.003.

66. Bialkowska, A.B., Yang, V.W., and Mallipattu, S.K. (2017). Kruppel-like factors in mammalian stem cells and development. Development *144*, 737–754. https://doi.org/10.1242/dev.145441.

67. Ando, T., Ishiguro, H., Kimura, M., Mitsui, A., Mori, Y., Sugito, N., Tomoda, K., Mori, R., Harada, K., Katada, T., et al. (2007). The overexpression of caveolin-1 and caveolin-2 correlates with a poor prognosis and tumor progression in esophageal squamous cell carcinoma. Oncol. Rep. *18*, 601–609.

68. Tadokoro, T., Tanaka, K., Osakabe, S., Kato, M., Kobayashi, H., Hogan, B.L.M., and Taniguchi, H. (2021). Dorso-ventral heterogeneity in tracheal basal stem cells. Biol. Open *10*, bio058676. https://doi.org/10.1242/bio.058676.

69. Bolton, S.J., Pinnion, K., Oreffo, V., Foster, M., and Pinkerton, K.E. (2009). Characterisation of the proximal airway squamous metaplasia induced by chronic tobacco smoke exposure in spontaneously hypertensive rats. Respir. Res. *10*, 118. https://doi.org/10.1186/1465-9921-10-118.

70. Lin, B., Shah, V.S., Chernoff, C., Sun, J., Shipkovenska, G.G., Vinarsky, V., Waghray, A., Xu, J., Leduc, A.D., Hintschich, C.A., et al. (2024). Airway hillocks are injury-resistant reservoirs of unique plastic stem cells. Nature *629*, 869–877. https://doi.org/10.1038/s41586-024-07377-1.

71. Han, J., Back, S.H., Hur, J., Lin, Y.H., Gildersleeve, R., Shan, J., Yuan, C.L., Krokowski, D., Wang, S., Hatzoglou, M., et al. (2013). ER-stress-induced transcriptional regulation increases protein synthesis leading to cell death. Nat. Cell Biol. *15*, 481–490. https://doi.org/10.1038/ncb2738.

72. Oyadomari, S., and Mori, M. (2004). Roles of CHOP/GADD153 in endoplasmic reticulum stress. Cell Death Differ. *11*, 381–389. https://doi.org/10.1038/sj.cdd.4401373.

73. Kale, J., Osterlund, E.J., and Andrews, D.W. (2018). BCL-2 family proteins: changing partners in the dance towards death. Cell Death Differ. *25*, 65–80. https://doi.org/10.1038/cdd.2017.186.

74. Singh, R., Letai, A., and Sarosiek, K. (2019). Regulation of apoptosis in health and disease: the balancing act of BCL-2 family proteins. Nat. Rev. Mol. Cell Biol. *20*, 175–193. https://doi.org/10.1038/s41580-018-0089-8.

75. Gross, A., McDonnell, J.M., and Korsmeyer, S.J. (1999). BCL-2 family members and the mitochondria in apoptosis. Genes Dev. *13*, 1899–1911. https://doi.org/10.1101/gad.13.15.1899.

76. Naim, S., and Kaufmann, T. (2020). The Multifaceted Roles of the BCL-2 Family Member BOK. Front. Cell Dev. Biol. *8*, 574338. https://doi.org/10.3389/fcell.2020.574338.

77. Carpio, M.A., Michaud, M., Zhou, W.P., Fisher, J.K., Walensky, L.D., and Katz, S.G. (2015). BCL-2 family member BOK promotes apoptosis in response to endoplasmic reticulum stress. Proc. Natl. Acad. Sci. USA *112*, 7201–7206. https://doi.org/10.1073/pnas.1421063112.

78. Fernanda de Mello Costa, M., Weiner, A.I., and Vaughan, A.E. (2020). Basal-like Progenitor Cells: A Review of Dysplastic Alveolar Regeneration and Remodeling in Lung Repair. Stem Cell Rep. *15*, 1015–1025. https://doi.org/10.1016/j.stemcr.2020.09.006.

79. Xi, Y., Kim, T., Brumwell, A.N., Driver, I.H., Wei, Y., Tan, V., Jackson, J.R., Xu, J., Lee, D.K., Gotts, J.E., et al. (2017). Local lung hypoxia determines epithelial fate decisions during alveolar regeneration. Nat. Cell Biol. *19*, 904–914. https://doi.org/10.1038/ncb3580.

80. Weiner, A.I., Zhao, G., Zayas, H.M., Holcomb, N.P., Adams-Tzivelekidis, S., Wong, J., Gentile, M.E., Reddy, D., Wei, J., Palashikar, G., et al. (2022). DeltaNp63 drives dysplastic alveolar remodeling and restricts epithelial plasticity upon severe lung injury. Cell Rep. *41*, 111805. https://doi.org/10.1016/j.celrep.2022.111805.

81. Chen, W.D., and Miao, C.L. (2022). KRT15 promotes colorectal cancer cell migration and invasion through β-catenin/MMP-7 signaling pathway. Med. Oncol. *39*, 68. https://doi.org/10.1007/s12032-021-01619-2.

82. Lie-a-Ling, M., Marinopoulou, E., Li, Y.Y., Patel, R., Stefanska, M., Bonifer, C., Miller, C., Kouskoff, V., and Lacaud, G. (2014). RUNX1 positively regulates a cell adhesion and migration program in murine hemogenic endothelium prior to blood emergence. Blood *124*, e11–e20. https://doi.org/10.1182/blood-2014-04-572958.

83. Sangpairoj, K., Vivithanaporn, P., Apisawetakan, S., Chongthammakun, S., Sobhon, P., and Chaithirayanon, K. (2017). RUNX1 Regulates Migration, Invasion, and Angiogenesis via p38 MAPK Pathway in Human Glioblastoma. Cell. Mol. Neurobiol. *37*, 1243–1255. https://doi.org/10.1007/s10571-016-0456-y.

Cell Stem Cell
Article

CellPress

84. Willrodt, A.H., Salabarria, A.C., Schineis, P., Ignatova, D., Hunter, M.C., Vranova, M., Golding-Ochsenbein, A.M., Sigmund, E., Romagna, A., Strassberger, V., et al. (2019). ALCAM Mediates DC Migration Through Afferent Lymphatics and Promotes Allospecific Immune Reactions. Front. Immunol. 10, 759. https://doi.org/10.3389/fimmu.2019.00759.

85. von Lersner, A., Droesen, L., and Zijlstra, A. (2019). Modulation of cell adhesion and migration through regulation of the immunoglobulin superfamily member ALCAM/CD166. Clin. Exp. Metastasis 36, 87–95. https://doi.org/10.1007/s10585-019-09957-2.

86. Shaykhiev, R., and Crystal, R.G. (2014). Early events in the pathogenesis of chronic obstructive pulmonary disease. Smoking-induced reprogramming of airway epithelial basal progenitor cells. Ann. Am. Thorac. Soc. 11 (suppl 5), S252–S258. https://doi.org/10.1513/AnnalsATS.201402-049AW.

87. Sauler, M., McDonough, J.E., Adams, T.S., Kothapalli, N., Barnthaler, T., Werder, R.B., Schupp, J.C., Nouws, J., Robertson, M.J., Coarfa, C., et al. (2022). Characterization of the COPD alveolar niche using single-cell RNA sequencing. Nat. Commun. 13, 494. https://doi.org/10.1038/s41467-022-28062-9.

88. Kikkawa, M. (2013). Big steps toward understanding dynein. J. Cell Biol. 202, 15–23. https://doi.org/10.1083/jcb.201304099.

89. Yuniati, L., van der Meer, L.T., Tijchon, E., van Ingen Schenau, D., van Emst, L., Levers, M., Palit, S.A.L., Rodenbach, C., Poelmans, G., Hoogerbrugge, P.M., et al. (2016). Tumor suppressor BTG1 promotes PRMT1-mediated ATF4 function in response to cellular stress. Oncotarget 7, 3128–3143. https://doi.org/10.18632/oncotarget.6519.

90. Lassot, I., Estrabaud, E., Emiliani, S., Benkirane, M., Benarous, R., and Margottin-Goguet, F. (2005). p300 modulates ATF4 stability and transcriptional activity independently of its acetyltransferase domain. J. Biol. Chem. 280, 41537–41545. https://doi.org/10.1074/jbc.M505294200.

91. Ameri, K., and Harris, A.L. (2008). Activating transcription factor 4. Int. J. Biochem. Cell Biol. 40, 14–21. https://doi.org/10.1016/j.biocel.2007.01.020.

92. Zhao, E., Ding, J., Xia, Y., Liu, M., Ye, B., Choi, J.H., Yan, C., Dong, Z., Huang, S., Zha, Y., et al. (2016). KDM4C and ATF4 Cooperate in Transcriptional Control of Amino Acid Metabolism. Cell Rep. 14, 506–519. https://doi.org/10.1016/j.celrep.2015.12.053.

93. Shan, J., Fu, L., Balasubramanian, M.N., Anthony, T., and Kilberg, M.S. (2012). ATF4-dependent regulation of the JMJD3 gene during amino acid deprivation can be rescued in Atf4-deficient cells by inhibition of deacetylation. J. Biol. Chem. 287, 36393–36403. https://doi.org/10.1074/jbc.M112.399600.

94. Hsu, S.Y., Kaipia, A., McGee, E., Lomeli, M., and Hsueh, A.J.W. (1997). Bok is a pro-apoptotic Bcl-2 protein with restricted expression in reproductive tissues and heterodimerizes with selective anti-apoptotic Bcl-2 family members. Proc. Natl. Acad. Sci. USA 94, 12401–12406. https://doi.org/10.1073/pnas.94.23.12401.

95. Fernandez-Marrero, Y., Ke, F., Echeverry, N., Bouillet, P., Bachmann, D., Strasser, A., and Kaufmann, T. (2016). Is BOK required for apoptosis induced by endoplasmic reticulum stress? Proc. Natl. Acad. Sci. USA 113, E492–E493. https://doi.org/10.1073/pnas.1516347113.

96. Echeverry, N., Bachmann, D., Ke, F., Strasser, A., Simon, H.U., and Kaufmann, T. (2013). Intracellular localization of the BCL-2 family member BOK and functional implications. Cell Death Differ. 20, 785–799. https://doi.org/10.1038/cdd.2013.10.

97. Carpio, M.A., Means, R.E., Brill, A.L., Sainz, A., Ehrlich, B.E., and Katz, S.G. (2021). BOK controls apoptosis by Ca(2+) transfer through ER-mitochondrial contact sites. Cell Rep. 34, 108827. https://doi.org/10.1016/j.celrep.2021.108827.

98. Harfe, B.D., Scherz, P.J., Nissim, S., Tian, H., McMahon, A.P., and Tabin, C.J. (2004). Evidence for an expansion-based temporal Shh gradient in specifying vertebrate digit identities. Cell 118, 517–528. https://doi.org/10.1016/j.cell.2004.07.024.

99. Lee, D.K., Liu, Y., Liao, L., Wang, F., and Xu, J. (2014). The prostate basal cell (BC) heterogeneity and the p63-positive BC differentiation spectrum in mice. Int. J. Biol. Sci. 10, 1007–1017. https://doi.org/10.7150/ijbs.9997.

100. Ebert, S.M., Dyle, M.C., Kunkel, S.D., Bullard, S.A., Bongers, K.S., Fox, D.K., Dierdorff, J.M., Foster, E.D., and Adams, C.M. (2012). Stress-induced skeletal muscle Gadd45a expression reprograms myonuclei and causes muscle atrophy. J. Biol. Chem. 287, 27290–27301. https://doi.org/10.1074/jbc.M112.374777.

101. Afshar, K., Gaboyan, S., Kasaraneni, N., Chin, J., Nilaad, S., Advani, I.N., Olay, J., Park, K., Pham, J., Patel, S., et al. (2023). Rapid Low-ischemic Time Lung Explant Tissue Collection at the University of California San Diego. Am. J. Resp. Crit. Care 207, A2271.

102. Quiros, P.M., Goyal, A., Jha, P., and Auwerx, J. (2017). Analysis of mtDNA/nDNA Ratio in Mice. Curr. Protoc. Mouse Biol. 7, 47–54. https://doi.org/10.1002/cpmo.21.

103. Langmead, B., and Salzberg, S.L. (2012). Fast gapped-read alignment with Bowtie 2. Nat. Methods 9, 357–359. https://doi.org/10.1038/nmeth.1923.

104. Trapnell, C., Williams, B.A., Pertea, G., Mortazavi, A., Kwan, G., van Baren, M.J., Salzberg, S.L., Wold, B.J., and Pachter, L. (2010). Transcript assembly and quantification by RNA-Seq reveals unannotated transcripts and isoform switching during cell differentiation. Nat. Biotechnol. 28, 511–515. https://doi.org/10.1038/nbt.1621.

105. Hao, Y., Hao, S., Andersen-Nissen, E., Mauck, W.M., 3rd, Zheng, S., Butler, A., Lee, M.J., Wilk, A.J., Darby, C., Zager, M., et al. (2021). Integrated analysis of multimodal single-cell data. Cell 184, 3573–3587.e29. https://doi.org/10.1016/j.cell.2021.04.048.

106. Alquicira-Hernandez, J., and Powell, J.E. (2021). Nebulosa recovers single cell gene expression signals by kernel density estimation. Bioinformatics 37, 2485–2487. https://doi.org/10.1093/bioinformatics/btab003.

107. Korsunsky, I., Millard, N., Fan, J., Slowikowski, K., Zhang, F., Wei, K., Baglaenko, Y., Brenner, M., Loh, P.R., and Raychaudhuri, S. (2019). Fast, sensitive and accurate integration of single-cell data with Harmony. Nat. Methods 16, 1289–1296. https://doi.org/10.1038/s41592-019-0619-0.

108. Qiu, X., Mao, Q., Tang, Y., Wang, L., Chawla, R., Pliner, H.A., and Trapnell, C. (2017). Reversed graph embedding resolves complex single-cell trajectories. Nat. Methods 14, 979–982. https://doi.org/10.1038/nmeth.4402.

109. Trapnell, C., Cacchiarelli, D., Grimsby, J., Pokharel, P., Li, S., Morse, M., Lennon, N.J., Livak, K.J., Mikkelsen, T.S., and Rinn, J.L. (2014). The dynamics and regulators of cell fate decisions are revealed by pseudotemporal ordering of single cells. Nat. Biotechnol. 32, 381–386. https://doi.org/10.1038/nbt.2859.

110. Fan, C., Chen, F., Chen, Y., Huang, L., Wang, M., Liu, Y., Wang, Y., Guo, H., Zheng, N., Liu, Y., et al. (2024). irGSEA: the integration of single-cell rank-based gene set enrichment analysis. Brief. Bioinform. 25, bbae243. https://doi.org/10.1093/bib/bbae243.

111. Kolde, R., Laur, S., Adler, P., and Vilo, J. (2012). Robust rank aggregation for gene list integration and meta-analysis. Bioinformatics 28, 573–580. https://doi.org/10.1093/bioinformatics/btr709.

CellPress

Cell Stem Cell
Article

STAR★METHODS

KEY RESOURCES TABLE

REAGENT or RESOURCE	SOURCE	IDENTIFIER
Antibodies		
rabbit anti-SCGB1A1	Seven Hills Bioreagents	WRAB-3950
goat anti-SCGB3A2	R&D Systems	AF3465
mouse anti-FOXJ1	eBioscience	14-9965-80
mouse anti-TRP63	Biocare Medical	CM163a
rabbit anti-KRT5	Biolegend	905501
chicken anti-KRT5	Biolegend	905901
rabbit anti-MUC5B	CLOUD-CLONE CORP.	PAA684Mu01
rabbit anti-pro-SFTPC	Millipore	AB3786
mouse anti-HOPX	Santa Cruz	sc-398703
mouse anti-E-cadherin	BD Transduction Laboratories	610181
mouse anti-Cytokeratin 17	Santa Cruz	sc-393002
mouse anti-Cytokeratin 13	Invitrogen	MA1-35542
rabbit anti-Cleaved Caspase-3	Cell Signaling Technology	9661
rabbit anti-ATF4	Cell Signaling Technology	11815
rabbit anti-p-eIF2α	Cell Signaling Technology	3597
rabbit anti-p-PERK	Invitrogen	PA5-102853
rabbit anti-CDKN1A	Sigma	ZRB1141
syrian hamster anti-PDPN	Developmental Studies Hybridoma Bank	8.1.1
rabbit anti-ATP5A1	Proteintech	14676-1-AP
rabbit anti-Cytochrome c	Abcam	ab133504
rabbit anti-ATF6	Proteintech	24169-1-AP
rabbit anti-LONP1	Proteintech	15440-1-AP
Cy3-conjugated goat anti-mouse	Jackson ImmunoResearch	115-165-003
Cy3-conjugated goat anti-rabbit	Jackson ImmunoResearch	111-165-144
AF488-conjugated goat anti-mouse	Invitrogen	A-11001
AF488-conjugated goat anti-rabbit	Invitrogen	A-11008
AF647-conjugated goat anti-syrian hamster	Invitrogen	A-21451
Cy3-conjugated goat anti-syrian hamster	Jackson ImmunoResearch	107-165-142
AF488-conjugated goat anti-chicken	Invitrogen	A32931
AF594-conjugated donkey anti-goat	Invitrogen	A-11058
AF488-conjugated donkey anti-rabbit	Invitrogen	A-21206
rabbit anti-LONP1	Cell Signaling Technology	28020
mouse anti-NDUFA9	Invitrogen	459100
rabbit anti-SDHA	Cell Signaling Technology	5839S
rabbit anti-UQCRB	Proteintech	10756-1-AP
mouse anti-COX I	Abcam	ab14705
rabbit anti-COX II	Proteintech	55070-1-AP
rabbit anti-ATP5A1	Proteintech	14676-1-AP
mouse anti-beta-Actin	Novus Biologicals	NB600-501
donkey anti-Mouse IgG IRDye 680RD	LI-COR	926-68072
donkey anti-Rabbit IgG IRDye 800CW	LI-COR	926-32213
Bacterial and virus strains		
Influenza A virus H1N1/PR8	American Type Culture Collection	VR-95PQ

Cell Stem Cell
Article

Continued

REAGENT or RESOURCE	SOURCE	IDENTIFIER
Biological samples		
Human lung explant tissue	University of California San Diego	https://pulmonary.ucsd.edu/research/labs-centers/lung-explant-project/index.html
Chemicals, peptides, and recombinant proteins		
Tamoxifen	Sigma	T5648
Naphthalene	Sigma	PHR1275
ISRIB	AdooQ	A14302
Critical commercial assays		
Click-it EdU Cell Proliferation Kit	Invitrogen	C10337
Multiplex Fluorescent v2 Assay Kit	Advanced Cell Diagnostics	323110
Seahorse XF Cell Mito Stress Test Kit	Agilent Bioscience	103015
MitoSOX Mitochondrial Superoxide Indicators	Invitrogen	M36008
Mitochondria Isolation Kit for Tissue	Thermo Scientific	89801
Pierce Silver Stain Kit	Thermo Scientific	24612
Deposited data		
Bulk RNA-seq and scRNA-seq	This paper	GEO: GSE230334
Western blot	This paper	Mendeley Data: DOI: https://doi.org/10.17632/2s96rkg6mr.1
Experimental models: Organisms/strains		
Mouse: *Shh^cre*: B6.Cg-*Shh^tm1(EGFP/cre)Cjt*/J	Clifford Tabin	JAX: 005622
Mouse: *Lonp1^flox*: C57BL/6N-*Lonp1^tm1a(EUCOMM)Hmgu*	Helmholtz Zentrum Muenchen	JAX:031874
Mouse: *Foxj1^creERT2*: C57BL/6-*Tg(FOXJ1-cre/ERT2)1Blh*	Brigid L Hogan	Rawlins et al.[56]
Mouse: *Trp63^creERT2*: 129S6/SvEvTac-*Trp63^tm1.1(cre/ERT2)Jxu*	Jianming Xu	Lee et al.[99]
Mouse: *Sox2^creERT2*: B6;129S-*Sox2^tm1(cre/ERT2)Hoch*/J	JAX	JAX:017593
Mouse: *Krt5^creERT2*: Cg-*Krt5^tm1.1(cre/ERT2)Blh*/J	JAX	JAX:029155
Mouse: *Scgb1a1^creERT2*: B6N.129S6(Cg)-*Scgb1a1^tm1(cre/ERT)Blh*/J	JAX	JAX:016225
Mouse: *R26R^LSL-tdTomato*: B6.Cg-*Gt(ROSA)26Sor^tm14(CAG-tdTomato)Hze*/J	JAX	JAX:007914
Mouse: *Ddit3^flox*: B6.Cg-*Ddit3^tm1.1lrt*/J	JAX	JAX:030816
Mouse: *Atf4^flox*: C57BL/6-*Atf4^tm1.1Cmad*/J	Christopher Adams	Ebert et al.[100]
Mouse: *Bok^flox*: 129X1/SvJ-*Bok^tm1.1Sgk*	Samuel G. Katz	Carpio et al.[77]
Oligonucleotides		
Primer sequences used for RT-qPCR	See Table S2 for a list of primer sequences	N/A
Software and algorithms		
Cell Ranger	10x Genomics	https://www.10xgenomics.com/support/software/cell-ranger/latest
Seurat v4	Satija Lab	https://satijalab.org/seurat/articles/get_started.html
Monocle 3	Trapnell lab	https://cole-trapnell-lab.github.io/monocle3/
irGSEA	Chuiqin Fan and Lian Ma	https://github.com/chuiqin/irGSEA
Bowtie2	Ben Langmead and Steven L Salzberg	https://bowtie-bio.sourceforge.net/bowtie2/manual.shtml
Cufflinks	Cole Trapnell and Lior Pachter	https://cole-trapnell-lab.github.io/cufflinks/

RESOURCE AVAILABILITY

Lead contact
Further information and requests for resources and reagents should be directed to and will be fulfilled by the lead contact, Xin Sun (xinsun@health.ucsd.edu).

Materials availability
This study did not generate new unique reagents.

Data and code availability
Bulk and single cell RNA-seq data have been deposited at the Gene Expression Omnibus and are publicly available as of the date of publication. Accession numbers are listed in the key resources table. Original western blot images have been deposited at Mendeley and are publicly available as of the date of publication. The DOI is listed in the key resources table. No custom code was generated in this study. Any additional information required to reanalyze the data reported in this paper is available from the lead contact upon request.

EXPERIMENTAL MODEL AND SUBJECT DETAILS

Mice
Shh^{cre}, [98] $Lonp1^{flox}$, [42] $Foxj1^{creERT2}$ [56] and $Trp63^{creERT2}$ [99] mice have been described previously. $Sox2^{creERT2}$ (#017593), $Krt5^{creERT2}$ (#029155), $Scgb1a1^{creERT2}$ (#016225), $R26R^{LSL-tdTomato}$ (#007914) and $Ddit3^{flox}$ (#030816) mice were purchased from JAX. $Atf4^{flox}$ was a kind gift from Dr. Michael Karin at UCSD with permission from Dr. Christopher Adams at University of Iowa. [100] Bok^{flox} mice were a kind gift from Dr. Samuel G. Katz at Yale University. [77] Embryos used in this study were harvested from time-mated mice, counting noon of the day when the vaginal plug was found as E0.5. All mice were in B6 background or have been back crossed to B6 background for at least 3 generations. Littermates were used as controls in all experiments. Both males and females were randomly assigned to experimental groups. Tamoxifen (T5648, Sigma) dissolved in corn oil was administrated intraperitoneally at a dose of 50 mg/kg. For continuous tamoxifen administration in $Foxj1creER;Lonp1$, tamoxifen was delivered every other day from D0 to D60. Mice aged between 8 to 10 weeks were treated with naphthalene (PHR1275, Sigma) at a dose of 275 mg/kg body weight during 9-10 AM in the morning. ISRIB (A14302, AdooQ) was dissolved in DMSO at 4.17 mg/ml and subsequently diluted in corn oil at 0.25 mg/ml as working solution. Mice were administrated intraperitoneally at the dose of 2.5 mg/kg every other day following the last dose of tamoxifen until lung harvesting. All mice were housed in facilities accredited by American Association for Accreditation of Laboratory Animal Care (AAALAC) at University of California San Diego. All animal husbandry and experiments were approved by the Institutional Animal Care and Use Committee (IACUC).

Human donors and tissue collection
Disease lung samples were obtained from diagnosed COPD patients who underwent lung transplantation. Tissues were collected rapidly (within 15 minutes post explant) to minimize ischemic time and preserve gene expression. [101] Lobectomy tissues without pathological lesion were collected as controls (n=3, non-COPD lobectomy controls). Sample details were listed in Table S1. All procedures for procuring human lung samples were IRB approved by the University of California San Diego Human Research Protections Program. Informed consent was obtained for all procedures. Immunostaining was performed on paraformaldehyde fixed, paraffin embedded lung samples.

METHOD DETAILS

Tissue preparation and immunofluorescent staining
Tracheas and lungs from embryos or adults were fixed in 4% paraformaldehyde (Electron Microscopy Sciences) diluted in PBS overnight at 4°C. Samples were embedded in either paraffin or OCT (Electron Microscopy Sciences) for sectioning. Antigen retrieval was performed before serum-mediated blocking by using high-PH retrieval buffer (10 mM Tris, 1 mM EDTA, pH 9.0). Primary antibodies with final concentrations used for immunofluorescence staining are: rabbit anti-SCGB1A1 polyclonal antibody [5 mg/ml] (WRAB-3950, Seven Hills Bioreagents), goat anti-SCGB3A2 Polyclonal antibody [5 mg/ml] (AF3465, R&D Systems), mouse anti-FOXJ1 monoclonal antibody [8 mg/ml] (14-9965-80, eBioscience), mouse anti-TRP63 monoclonal antibody [8 mg/ml] (CM163a, Biocare Medical), rabbit anti-KRT5 polyclonal antibody [5 mg/ml] (905501, Biolegend), chicken anti-KRT5 polyclonal antibody [5 mg/ml] (905901, Biolegend), rabbit anti-MUC5B polyclonal antibody [10 mg/ml] (PAA684Mu01, CLOUD-CLONE CORP.), rabbit anti-pro-SFTPC polyclonal antibody [8 mg/ml] (AB3786, Millipore), mouse anti-HOPX monoclonal antibody [5 mg/ml] (sc-398703, Santa Cruz), mouse anti-E-cadherin monoclonal antibody [5 mg/ml] (610181, BD Transduction Laboratories), mouse anti-Cytokeratin 17 monoclonal antibody [8 mg/ml] (sc-393002, Santa Cruz), mouse anti-Cytokeratin 13 monoclonal antibody [5 mg/ml] (MA1-35542, Invitrogen), rabbit anti-Cleaved Caspase-3 polyclonal antibody [5 mg/ml] (9661, CST), rabbit anti-ATF4 monoclonal antibody [5 mg/ml] (11815, CST), rabbit anti-p-eIF2α monoclonal antibody [5 mg/ml] (3597, CST), rabbit anti-p-PERK polyclonal antibody [5 mg/ml] (PA5-102853, Invitrogen), rabbit anti-CDKN1A monoclonal antibody [5 mg/ml] (ZRB1141, Sigma), syrian hamster

Cell Stem Cell
Article

CellPress

anti-PDPN polyclonal antibody [5 mg/ml] (8.1.1, Developmental Studies Hybridoma Bank), rabbit anti-ATP5A1 polyclonal antibody [10 mg/ml] (14676-1-AP, Proteintech), rabbit anti-Cytochrome c monoclonal antibody [5 mg/ml] (ab133504, Abcam), rabbit anti-ATF6 polyclonal antibody [10 mg/ml] (24169-1-AP, Proteintech) and rabbit anti-LONP1 polyclonal antibody [8 mg/ml] (15440-1-AP, Proteintech). The following secondary antibodies were used with final concentration: Cy3-conjugated goat anti-mouse IgG [2 mg/ml] (115-165-003, Jackson ImmunoResearch), Cy3-conjugated goat anti-rabbit IgG [2 mg/ml] (111-165-144, Jackson ImmunoResearch), AF488-conjugated goat anti-mouse IgG [2 mg/ml] (A-11001, Invitrogen), AF488-conjugated goat anti-rabbit IgG [2 mg/ml] (A-11008, Invitrogen), AF647-conjugated goat anti-syrian hamster IgG [2 mg/ml] (A-21451, Invitrogen), Cy3-conjugated goat anti-syrian hamster IgG [2 mg/ml] (107-165-142, Jackson ImmunoResearch), AF488-conjugated goat anti-chicken IgG [2 mg/ml] (A32931, Invitrogen), AF594-conjugated donkey anti-goat IgG [2 mg/ml] (A-11058, Invitrogen), AF488-conjugated donkey anti-rabbit IgG [2 mg/ml] (A-21206, Invitrogen). All images were acquired on the ZEISS AxioImager 2, except for slide scans on Olympus SLIDEVIEW VS200. 20X or 40X IF images were used to quantify cells labeled by specific markers. For each condition, at least 3 sections per mouse, and 3 mice per genotype were analyzed.

EdU analysis for cell proliferation
Click-it EdU Cell Proliferation Kit (C10337, Invitrogen) was used to measure the proliferation signal. For EdU analysis in embryos, 1 ml of 400 mM EdU solution (diluted in PBS, Invitrogen) was intraperitoneally injected into pregnant females. Lungs were harvested 2 hours post injection. Samples were fixed in 4% PFA overnight at 4°C before incubation in 30% sucrose followed by OCT embedding.

RNAscope
Multiplex Fluorescent v2 Assay Kit (323110, ACD) was used to detect *Lonp1, Atf4* and *Bok* RNAs. 4% PFA fixed-frozen sample were prepared and processed following the RNAscope protocol. *Lonp1* RNA probe (#497251), *Atf4* RNA probe (#405101) and *Bok* RNA probe (#801861-C2) were purchased from ACD. RNA probes stained with the Opal 570 fluorophore were then counter stained with DAPI and one of the FOXJ1/SCGB1A1/TRP63/KRT5 antibodies accordingly.

Mitochondrial DNA copy number analysis
Analysis of the mitochondrial DNA copy number is performed according to published protocol.[102] Briefly, embryos at E13.5 were harvested and subjected to total DNA extraction. Two pairs of qPCR primers specific to mitochondrial DNA (mtDNA) were used for quantification by qPCR: a) 16S rRNA, FWD: 5''-CCGCAAGGGAAAGATGAAAGAC-3', REV: 5'-TCGTTTGGTTTCGGGGGTTTC-3' b) ND1, FWD: 5'-CTAGCAGAAACAAACCGGGC-3', REV: 5'-CCGGCTGCGTATTCTACGTT-3'. Nuclear DNA (nDNA) specific gene HK2 (FWD: 5'-GCCAGCCTCTCCTGATTTTAGTGT-3', REV: 5'-GGGAACACAAAAGACCTCTTCTGG-3') was used for normalization. The final ratio of mtDNA/nDNA was used as the readout for mtDNA copy number variation.

Mitochondrial ROS measurement by MitoSOX
The specific detection and measurement of mitochondrial ROS in embryonic epithelium was conducted by using MitoSOX Red mitochondrial superoxide indicator (Invitrogen). Embryonic lungs at E13.5 were harvested and dissociated in the lysis buffer (PRMI 1640 (Thermo Scientific) with 10% FBS, 1 mM HEPES (Life Technology), 1 mM MgCl2 (Life Technology), 1 mM CaCl2 (Sigma-Aldrich), 0.525 mg/ml collagenase D (Roche), 5 unit/ml Dispase (Stemcell Technologies) and 0.05 mg/ml DNase I (Roche)). Incubation of the lysate on the rotator at 150 rpm at 37°C for 15 min, followed by the removal of red blood cells by RBC lysis buffer (Biolegend). Remaining cells were resuspended and blocked by FcBlock antibody (5 mg/ml, BD) for 10 min at RT. The following antibodies were added to label the corresponding cells: CD326-APC (118213, Biolegend) for epithelial cells, CD31-AF700 (102444, Biolegend) for endothelial cells, CD45-BV510 (103137, Biolegend) for immune cells, Ghost dye red 780 for cell viability (13-0865, TONBO) and the MitoSOX. After 20 min incubation at RT, cells were fixed with the BD stabilizing fixative and kept at 4°C until FACS. FlowJo software (BD) was used to analyze the acquired data.

Mitochondrial OCR analysis
The Oxygen Consumption Rate (OCR) of airway epithelial cells was measured by the Seahorse platform (XF96 extracellular flux analyser, Agilent Bioscience). Briefly, trachea and extrapulmonary bronchi were harvested from *Sox2creER;Lonp1* and control adult mice at D8 post tamoxifen administration. Cell suspension was prepared according to the lung dissociation protocol described elsewhere in the method. After blocking with the Fc Block Reagents (553141, BD Biosciences), cells were incubated with biotin conjugated CD31 (553371, BD Biosciences) and CD45 (553078, BD Biosciences) antibodies. These biotin-labeled cells were completely removed by streptavidin conjugated magnetic beads (19860, STEMCELL). Next epithelial cells were labeled with biotin conjugated EPCAM antibody (13-5791-82, Invitrogen), and were isolated by magnetic beads.

2.0×10^4 epithelial cells were seeded each well on the Agilent 96-well plate precoated by Cell-Tak (354240, Corning). Basal mitochondrial respiration was calculated by subtracting the non-mitochondrial OCR, acquired with 0.5 μM Rotenone (R8875, Sigma), from baseline OCR. Coupled mitochondrial respiration was calculated by subtracting the OCR in the treatment of 1.5 μM oligomycin (75351, Sigma) from baseline OCR. Data were analyzed with Agilent Seahorse Wave software (v.2.6).

Mitochondria isolation and protein fractionation

Pooled embryonic lungs of *Shhcre;Lonp1* and control mice (6 for each) at E13.5 were used for isolating mitochondria using Mitochondria Isolation Kit for Tissue (89801, Thermo Scientific) according to the manufacturer's protocol. Mitochondria pellets were resuspended in TBS buffer with 0.05% Triton X-100, and the total mitochondrial proteins were immediately aliquoted for future use. After incubation on ice for 20 min, the insoluble protein fractions were separated from soluble fractions by centrifuge at 13,600 rpm for 15 min. Total and insoluble protein fractions were further dissolved in RIPA buffer (9806, CST) supplemented with protease inhibitors (11697498001, Roche). Protein concentration of each fraction was measured by Pierce BCA Protein Assay kit (23225, Thermo Scientific), and followed by protein electrophoresis on a 4%–12% SDS-PAGE gel (NP0321BOX, Invitrogen). Silver staining was performed using Pierce Silver Stain Kit (24612, Thermo Scientific) according to the manufacturer's protocol.

Quantitative PCR (qPCR)

Total RNA from embryonic and adult lungs were extracted by using Trizol (Invitrogen) and RNeasy Micro RNA extraction kit (Qiagen). Reverse transcription was then carried out to obtain corresponding cDNA using iScript Select cDNA Synthesis Kit (Bio-Rad). qPCR master mix was prepared using SYBR Green reagents (Bio-Rad) and amplification signals were obtained by CFX ConnectTM system (Bio-Rad). At least three biological replicates were assayed for each gene unless otherwise noted. Primers used for qPCR analysis are listed in Table S2.

Western blot analysis

Embryonic lungs at E13.5 were collected in RIPA Lysis and Extraction Buffer (9806, CST) supplemented with cOmplete Protease Inhibitor Cocktail tablets (11697498001, Roche). Samples were homogenized in a QIAGEN TissueLyser II and proteins were purified from the supernatant after high-speed centrifugation. Protein concentrations were measured by Pierce BCA Protein Assay kit (23225, Thermo Scientific). 10 μg protein sample was loaded in each well and run on a 4%–12% SDS-PAGE gel (NP0321BOX, Invitrogen), then transferred to the nitrocellulose membrane (1620112, 0.2 μm, Bio-Rad) by the Trans-Blot Turbo Transfer System (Bio-Rad). Then the membranes were blocked in TBST (0.1% Tween-20) with 5% BSA for 1.5 hours at room temperature (RT) before incubation in primary antibodies overnight at 4°C. After 3 rounds of washing with TBST, membranes were incubated in the secondary antibody for 1 hour at RT. Images were acquired by Odyssey DLx Imager (LI-COR) and quantified by ImageJ. The following primary antibodies were used: LONP1 (28020, CST, 1:1000), NDUFA9 (459100, Invitrogen, 1:1000), SDHA (5839S, CST, 1:1000), UQCRB (10756-1-AP, Proteintech, 1:1000), COX I (ab14705, Abcam, 1:500), COX II (55070-1-AP, Proteintech, 1:1000), ATP5A1 (14676-1-AP, Proteintech, 1:500) and beta-Actin (Novus Biologicals, NB600-501, 1:5000). Secondary antibodies used were: donkey anti-Mouse IgG IRDye 680RD (LI-COR, 926-68072, 1:10000) and donkey anti-Rabbit IgG IRDye 800CW (LI-COR, 926-32213, 1:10000). Three biological replicates were analyzed for each condition or genotype.

Bulk RNA-seq and data analysis

Total RNA from embryonic lungs at E13.5 were extracted as described above. cDNA libraries were constructed using Illumina TruSeq RNA Library Prep Kit V2 (Illumina) and sequenced on the HiSeq4000 platform (Illumina) at the Institute for Genomic Medicine (IGM) at UCSD. FASTQ files were aligned to the mouse reference genome (mm10) by using Bowtie2[103] with default settings. Differential gene expression analysis was performed using Cufflinks.[104] Heatmaps and volcano plots were generated by ggplot2 (version 3.3.2).

Tissue dissociation and sorting of epithelial cells

Sox2creER;Lonp1;tdTomato and the corresponding control mice at 39 days post *Lonp1* inactivation were used for cell dissociation followed by scRNA-seq. Briefly, to remove the circulating blood cells, every mouse was transcardially perfused with 12 ml of cold DPBS (Life Technology) before harvest. Lungs were then inflated intratracheally with cold lysis buffer (recipe referred to the mitoSOX method). Trachea and lungs from control mice, and lungs without trachea and extrapulmonary bronchi from *Lonp1* mutant mice, were chopped into the lysis buffer and mechanically homogenized by GentleMACS dissociator (Miltenyi Biotec). Tissues were further incubated in the lysis buffer on the rotator (150 rpm) for 30 min at 37°C, then filtered through a 70 μm MACS SmartStrainer. Red blood cells were removed by ACK lysis buffer (A1049201, Gibco). Cells were further collected by centrifugation at 1500 rpm at 4°C for 5 min (acceleration/deceleration=7), counted with a hemocytometer and then diluted to ~1X10^6 cells per ml. After blocking with FcBlock antibody (5 mg/ml) for 10 min at RT, endothelial cells and immune cells were labeled with biotinylated CD31 (13-0311-82, eBioscience) and CD45 (13-0451-82, eBioscience) antibodies respectively, and removed by the magnet-mediated EasySep Cell Isolation technology (19860, STEMCELL). The remaining cells were stained with APC-Cy7 conjugated anti-CD326 (G8.8, Biolegend) and DAPI (D9542, Sigma). Epithelial cells were sorted and collected as DAPI-;CD326(EPCAM)+;tdTomato+ on a FACSAria II high speed sorter (BD Biosciences).

Same protocols were utilized for cell dissociation in the lungs (without trachea and extrapulmonary bronchi) injured by influenza infection. To enable the final acquirement of similar cell numbers from epithelial and mesenchymal compartments of the lung, sorted cells are reproportioned in the ratio of 2:1 (epithelium: mesenchyme) before library construction.

Single-cell RNA-seq and data analysis

Following FACS, single cell libraries were generated from sorted cells by using Chromium Single Cell 3' v3 kit (10X Genomics). Sequencing was carried out on the NovaSeq (Illumina) platform at IGM, UCSD. For data analysis, Cell Ranger (version 3.0.2) was

Cell Stem Cell
Article

CellPress

used to initially align the raw reads onto the mouse reference genome (mm10) and generate the feature-barcode matrix. Next, R package Seurat (version 4.0)[105] was used to perform data quality control, normalization, scaling, principal components analysis (PCA) and the canonical correlation analysis (CCA) based data integration. Briefly, to filter out low-quality cells or doublets, cells with fewer than 200 or more than 4,000 unique features, or more than 15% mitochondrial contents were removed from further analysis. Then "LogNormalize" was used to normalize the feature expression. A total of 2,000 top variable features were identified by function FindVariableFeatures and kept for PCA. Top 20 significant components were chosen to conduct dimensional reduction by uniform manifold approximation and projection (UMAP) with default parameters. The expression features of marker genes were profiled and visualize by R package ggplot2 (version 3.3.2). Density plots were generated by R package Nebulosa (1.0.2).[106] Integration of flu injured cells are accomplished by Harmony algorithm.[107] Lineage trajectory analysis was performed by Monocle 3[108,109] using resolution = 1e-3 in the step of cell clustering.

To determine the proper threshold for purifying *bona fide* basal cells used in Figures S3P–S3S, general basal cell cluster in the integrated dataset was further subclustered. These cells were filtered against low-quality basal signatures by requiring expressions of two key gene factors, *Krt5* and *Trp63*. Applying normalized expression cutoffs from "*Krt5* > 0 or *Trp63* > 0" to "*Krt5* > 1 or *Trp63* > 1", we found that the proportion of bona fide basal cells were gradually increased to near 100%, at the cost of losing their absolute cell numbers as dropped off with other *Krt5*/*Trp63* low or negative cells. At *Krt5* > 0.5 or *Trp63* > 0.5, most of the *Krt5*-low and *Trp63*-low cells were removed (26 out of 32), and a majority of *bona fide* basal cells were retained (153 out of 163). This balanced cutoff was therefore chosen for following analysis.

Pathway enrichment analysis
Gene set enrichment analysis in single cells was carried out by using the R package irGSEA.[110] The enrichment of pathways in KEGG and Reactome was initially scored for individual cells by using four different gene set enrichment methods (AUCell, UCell, Singscore and Ssgsea). Next Wilcox test was performed to all enrichment score matrices and gene sets with adjusted p value < 0.05 were used to integrate through R package Robust Rank Aggregation (version 1.2.1).[111] Density scatterplot of enriched pathway scores (AUCell) on the UMAP was generated by R package Nebulosa (1.0.2).

Influenza PR8 infection
Mouse adapted influenza strain H1N1/PR8 was obtained from ATCC (VR-95PQ) and used in all viral infection. Both male and female mice between 10-12 weeks were used. Deep mouse anesthesia was achieved by ketamine-xylazine (K, 100 mg/kg; X, 10 mg/kg) injection. PR8 was intranasally administrated at a dose of ∼0.5 LD_{50} in a total volume of 35 μL per mouse. PBS is used for virus dilution and delivered in the same way to the control group. To preempt the influence of baseline phenotypes associated with long-term loss of *Lonp1*, both *Sox2creER;Lonp1* mutant and control mice were subjected to virus inoculation just 4 days after the last injection of tamoxifen, and lungs were analyzed 14 days post infection. All procedures were conducted in the BSL2 facility at UCSD.

QUANTIFICATION AND STATISTICAL ANALYSIS

For quantification using sections, 3 sections per sample were analyzed. The sections were selected from equivalent depths from sample to sample. Different quantification methods were used based on the nature of the data, as noted in individual figure legend. One-way ANOVA Tukey's multiple comparisons test, Wilcox test or Student's t test were used depending on data types. All statistical analyses were performed using Prism 9 (GraphPad). Significance in the Figures: ns, not significant, $p > 0.05$; * for $p < 0.05$; ** for $p < 0.01$. Error bars represent mean ± SD.